I.FAST

Innovation Fostering in Accelerator Science and Technology

Horizon 2020 Research Infrastructures GA n° 101004730

DELIVERABLE REPORT

Conceptual Design of combined CCT in LTS

DELIVERABLE: D8.2

Document identifier:	IFAST-D8.2
Due date of deliverable:	End of Month 10 (February 2022)
Justification for delay:	Completion of the calculations
Report release date:	21/02/2022
Work package:	WP8:Innovative Superconducting Magnets
Lead beneficiary:	INFN
Document status:	Final

ABSTRACT

The following report presents the conceptual design study of the combined Canted Cosine Theta (CCT) magnet made using the Low Temperature Superconductor (LTS) Niobium-Titanium (NbTi). The report highlights the complete lists of parameters (target, superconductor, cable and CCT geometry), motivating the choice for the design. The magnetic and mechanical design are presented in the second and third section. A protection study is reported in the fourth section, highlighting the capability given by the rope cable. In the fifth section a preliminary evaluation of the main power losses has been done, focusing the attention on the conductor (persistent currents and interfilament coupling currents losses) and metallic former losses (eddy currents).

IFAST Consortium, 2021

For more information on IFAST, its partners and contributors please see https://ifast-project.eu/

This project has received funding from the European Union's Horizon 2020 Research and Innovation programme under Grant Agreement No 101004730. IFAST began in May 2021 and will run for 4 years.

Delivery Slip

	Name	Partner	Date
Authored by	E. De Matteis, G. Ceruti, S. Mariotto, M. Prioli, S. Sorti	INFN	18/02/2022
Edited by	E. De Matteis	INFN	18/02/2022
Reviewed by	M. Statera	INFN	18/02/2022
Approved by	L. Rossi (WP8 Coordinator) M. Vretenar (Project Coordinator)	INFN CERN	21/02/2022

TABLE OF CONTENTS

1. INTRODUCTION 5

2. LIST OF PARAMETERS 6

2.1 TARGET PARAMETERS 6
2.2 NBTI SUPERCONDUCTOR 7
2.3 CABLE PARAMETERS 8
2.4 CCT – INNER AND OUTER LAYERS PARAMETERS 9

3. MAGNETIC DESIGN AND FIELD QUALITY 12

3.1 3D MAGNETIC DESIGN 12
3.2 FIELD QUALITY 15

4. MECHANICAL DESIGN 16

4.1 DESCRIPTION OF THE MECHANICAL STRUCTURE 17
4.2 MECHANICAL SIMULATIONS 19
4.2.1 Constraints: 20
4.2.2 Materials 21
4.2.3 Simulations Results 23

5. STABILITY AND PROTECTION 27

6. POWER LOSSES 31

6.1 CONDUCTOR LOSSES 31
6.1.1 Persistent Currents Magnetization Loss 31
6.1.2 Interfilament Coupling Currents Loss 32
6.1.3 Total conductor losses 33
6.2 METALLIC FORMER LOSSES 34
6.2.1 Inner layer eddy current losses 35
6.2.2 Outer former eddy current losses 35
6.2.3 Evaluation of former eddy current power losses 36
6.3 CURRENT LEADS POWER CONSUMPTION 38

7. CONCLUSIONS AND FUTURE PLANS 39

8. REFERENCES 41

Executive summary

The conceptual design report presented represents a preliminary study of the combined Canted Cosine Theta (CCT) demonstrator in NbTi from the magnetic, mechanical, protection and power losses point of view

The list of the parameters (target, superconductor, cable and CCT inner and outer layers) have been presented, motivating the design choice for the majority of the values.

The magnetic design section shows how the magnet achieves the target dipole (4 T of bore field) and quadrupole fields (5 T/m of gradient), at nominal current @ 4.7 K temperature. The load line margin is 28.7% @4.7 K and 33.4% @4.2 K, bigger than the target 25% @4.7 K; the critical temperature is 6.3 K (with a temperature margin of about 1.6 K). The magnetic length is of about 0.73 m, slightly less than target 0.8 m, which is due to limitation of the total physical length of the magnet to 1 m. The field quality shows 6 units of b3, not critical at this stage, but is certainly an aspect to be further improved.

The mechanical design presents a full description of the mechanical structure. The materials simulated for the former are aluminium bronze 954 and PEEK GF30 (polyether-ether-ketone reinforced with 30% of glass fibres). The stresses on the formers are well below the limit of both materials, resulting in a safety factor of 1.67 for PEEK GF 30 and 2.37 for aluminium bronze 954. The stresses on the conductor are far from the yield limit of 300 MPa of Nb-Ti. In case of aluminium bronze 954, the radial displacements are of the order of 10 µm, while for PEEK GF30 they are of about 100 µm (to be verified if critical or not). Azimuthal displacements have been evaluated but they remain well below the 100 µm for both the materials.

The protection section highlights that the time margins are larger (0.325 s for a rope 6 NbTi+1 copper strands, and 0.149 s for a rope 7 NbTi strands) compared to a high field magnet (100 ms for NbTi magnets, and 50 ms for Nb3Sn ones). The rope (6 NbTi +1 copper strands) has a 17% more limit than the 7 NbTi strands in terms of Quench Integral (QI). Both solutions are possible, we have selected 6+1 to increase stability.

For ramped field (0.4 T/s), the conductor losses due to persistent and interfilament coupling currents, are bigger than 2 W/m at low field (0.45 T), while are less than 1 W/m at 4 T. The eddy currents losses from the metallic former are the most significant ones, especially if the bulk formers are considered (13 W/m for the aluminium bronze). The best solution could be to use the aluminium-bronze for the former with a longitudinal cut on the pole, in order to keep the power losses to be dissipated in the order of 2 W/m, but this solution needs to be proved and for the moment is not pursued. The preliminary calculation of the current leads power consumption for a rope current of 1300 A gives 120 W of cooling power to be supplied at 50 K by one cryocooler.

A more detailed study covering all the open points will be done for the final Engineering Design report, however this report shows the feasibility of our demonstrator.

1. Introduction

Within the European project I.FAST, the Workpackage 8, Innovative superconducting magnets, has the main objective to advance HTS (High-Temperature Superconductivity) technology with CCT (Canted-Cosine Theta) layout, in a collaborative way between scientific institutes and industry. To this end the final goal is to manufacture an HTS CCT demonstrator of about 5 T. However, this demonstrator will be preceded by a simpler magnet in LTS (Low-Temperature Superconductivity) to develop competences and expertise [1].

Initially this first magnet had been foreseen to be curved, for use in compact synchrotrons or gantries for ion therapy of cancer. Since a curved Nb-Ti is in the scope of WP8 of the HITRI*plus* Integrating Activity project [7], which was not approved at the time of I.FAST submission, in agreement with the I.FAST Project Coordinator and Governing Board and in consultation with the Project Officer, the WP management has decided to focus instead on a "combined function" magnet as a first demonstrator. The combined function CCT has similar cost and complexity as the curved version and allows exploring the new and promising technology of combined function magnets crucial for applications in small accelerator systems for cancer therapy, at the same time avoiding any possible overlap with HITRIplus. The main feature of the demonstrator is that superimposed to the main dipole field of 4-5 T there will be a quadrupolar component of 5-10 T/m which will yield about 0.5-1 T additional peak field [2].

The task 8.2 has the aim to implement a preliminary engineering design of this magnet and to procure the superconductor for the construction of the demonstrator exploring different options for the magnet structure and magnetic design at conceptual level for a combined Canted Cosine Theta (CCT) scaled demonstrator in NbTi.

Among the various options, with different structural and superconducting layout, examined to approach an achromatic beam transport, a co-wind of dipole and quadrupole in the same winding has been chosen. As baseline the design considers the NbTi with fine filaments for low losses, for two main reasons: the availability of the superconductor for low losses at INFN - LASA, reducing the timing of the purchase and making the construction of a ramped CCT feasible; secondly, compared to the Nb3Sn, the windability and flexibility of the NbTi is clearly superior [3-5].

The present document will present the conceptual design of a combined CCT in NbTi, highlighting the motivations of the design choices. The first section is dedicated to reporting the list of parameters motivating the choice for the design, in terms of target, superconductor, cable and inner and outer CCT layer parameters. The second section presents the magnetic design study and the field quality. The third section reports the mechanical design, with a description of the assembly and the analysis results in terms of stresses, radial and azimuthal deformations. The fourth section highlights the protection limits of the CCT demonstrator using a rope cable. The fifth section is focused on the main power loss sources of the conductor, eddy currents on the metallic formers, and current leads power consumption.

2. List of parameters

The following section reports the lists of magnet parameters and aims at motivating the design choices. The paragraph 2.1 reports the target parameters of the final demonstrator. The paragraph 2.2 presents the superconductor features, low losses NbTi strand [6]. The paragraph 2.3 is focused on the final cable parameters. Finally, the paragraph 2.4 highlights the CCT parameters of the inner and outer layers, especially the geometrical ones.

2.1 TARGET PARAMETERS

The geometry is established to be straight in order to easily compare the NbTi-based magnet performance with the other demonstrator based on HTS, i.e. avoid adding additional difficulties to the critical HTS demonstrator. Moreover, the winding will be combined in order to provide a dipole field with a superimposed quadrupole component (4 T + 5 T/m). The central magnetic field of 4 T, the bore diameter of 80 mm and the dB/dt ramp rate of 0.4 T/s have been established as common values among two other parallel programs (HITRIplus and SIGRUM) [7, 8] in order to compare the performance of the several demonstrators, i.e. the values are oriented on a carbon ions gantry application for hadron therapy (beam rigidity of $B^*\rho = 6.6$ Tm, where ρ, the curvature radius of the gantry, is equal to 1.65 m). The magnetic and physical length has been fixed to 0.8 and 1 m, respectively, in order to have a good compromise between the flat longitudinal field region and the cost of the demonstrator, i.e. longer magnet means more conductor and/or costs. The operation temperature of 4.7 K foresees that the magnet will be cooled in helium gas, as envisaged by the other programs mentioned above. The idea is to have a ramped magnet without liquid helium, which for biomedical installations results as an additional cost (liquefier) and further technological difficulty for a gantry. The loadline margin has been fixed to 25% at 4.7 K. Apart to be CCT, the magnet should have an iron yoke (cold iron) for two main motivations: first for shielding the stray fields and second as collar-support system (see mechanical design section). Table 1 reports the target parameters established for the combined CCT demonstrator in LTS.

Table 1. List of target parameters for the CCT demonstrator magnets

Parameters	**Values**	**unit**
Magnet type	CCT	-
Geometry	Straight, combined	-
Iron	Shield +support	-
Central magnetic field B_o	4	T
Magnetic and physical length	0.8 and 1	m
Bore diameter	80	mm
dB/dt	0.4	T/s
Operation temperature	4.7	K
Loadline margin (@4.7 K) static	25	%
Superconductor	NbTi	-

2.2 NbTi SUPERCONDUCTOR

For the first CCT demonstrator, a NbTi wire available by INFN-Milano-LASA has been fully qualified by INFN-Milano-LASA, CERN, and Unige [6]. The NbTi superconductor wire produced by Bruker EAS (Hanau, Germany) is a customized wire originally designed according to the specifications for the DISCORAP project (INFN – GSI collaboration) [9]. Two billets of wire have been produced LF001 and LF002 (divided in 30 and 29 spools, respectively). The wire is now available at INFN-Milano-LASA.

Table 2. NbTi conductor parameters

Parameters	**Values**	**unit**
Strand type	Round	-
Diameter	0.821	mm
(Cu/NoCu) α	1.36	-
Jc (5T @ 4.2 K)	2300	A/mm^2
Ic (5T @ 4.2 K)	516	A
RRR	135	-
Filament diameter	3.15	µm

As reported in Tab. 2, the wire has been found of low losses quality, with Nb-Ti filaments of the order of 3.15 um. The critical current is relatively low, Jc= 2297 A/mm2 @ 5T, 4.2 K, about 20% lower than the corresponding LHC wire (LHC02 or outer layer strand) [10], which is in line with expectation for fine filament low losses wires (see Fig.1). The RRR is pretty good, as expected, above 130.

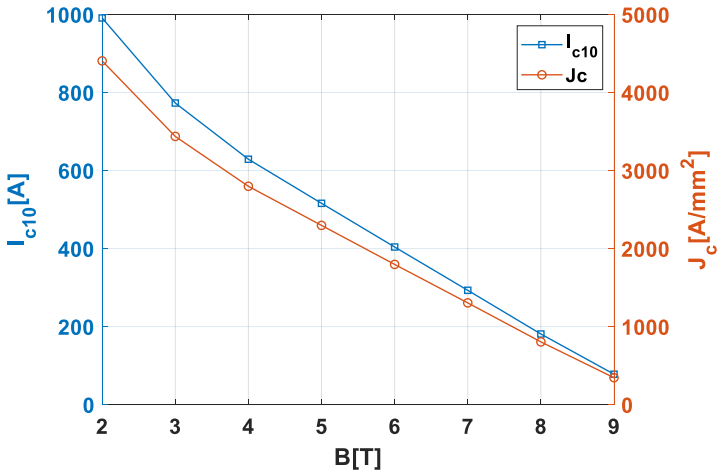

Figure 1. Critical current measurement I_{c10} (and current density J_c) with Electrical field criterion at 10uV/m @ 4.22 K.

2.3 CABLE PARAMETERS

The cable type is a twisted rope (6+1), i.e. composed of 6 NbTi wires twisted around a copper core wire (Fig. 2). The main reason for using a rope cable is to limit the operating current, offering the double advantage of a lower cost of the power converter and a reduction of the impact of the current leads on the cryogenics (see paragraph 6.3). The copper core has the double task, the first one is to be a mechanical support for the six twisted NbTi strands, and the second one is to increase the protection limits of the cable, as reported into the dedicated section (see Stability and Protection). The Table 3 reports the main design parameters of the chosen cable. The total current is the sum of the rope current in the groove, i.e. the ropes are connected in series. The insulation will be made by a double braid of polyester thread for a whole thickness of 0.12 mm. The twist pitch will be in the range of 30 ÷ 50 mm, depending on the rigidity of the produced rope.

Table 3. Cable parameters - Rope (6 NbTi wires +1 copper core wire)

Parameters	**Values**	**unit**
Type	Ropes (6+1)	-
Twist pitch	30 ÷ 50	mm
Rope current (4 T @4.7 K)	1308	A
Total current (4 T @4.7 K)	20928	A turns
J_{rope} (4 T @4.7 K)	275	A/mm^2
Insulating thickness	0.12	mm
J_{rope} (4 T @4.7 K) - insulated	228	A/mm^2
$J_{winding}$	161	A/mm^2

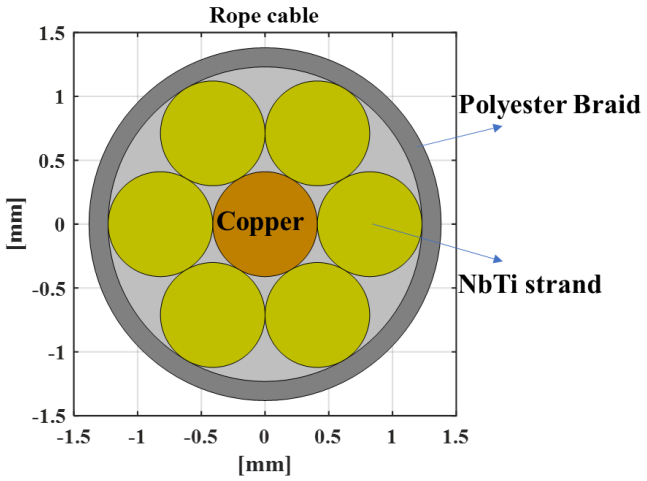

Figure 2. Cross section of the superconducting rope, 6 NbTi strands + 1 central copper strand.

2.4 CCT – INNER AND OUTER LAYERS PARAMETERS

The CCT design is based on pairs of windings around mandrels (also called formers) [11, 12] nested one inside other so that when the magnet is powered the transverse field components sum and axial field components cancel out (Fig. 3, left).

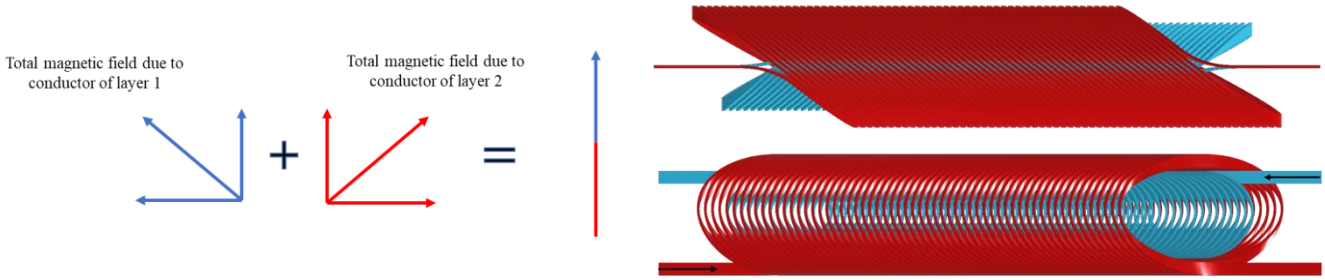

Figure 3. CCT field direction and winding.

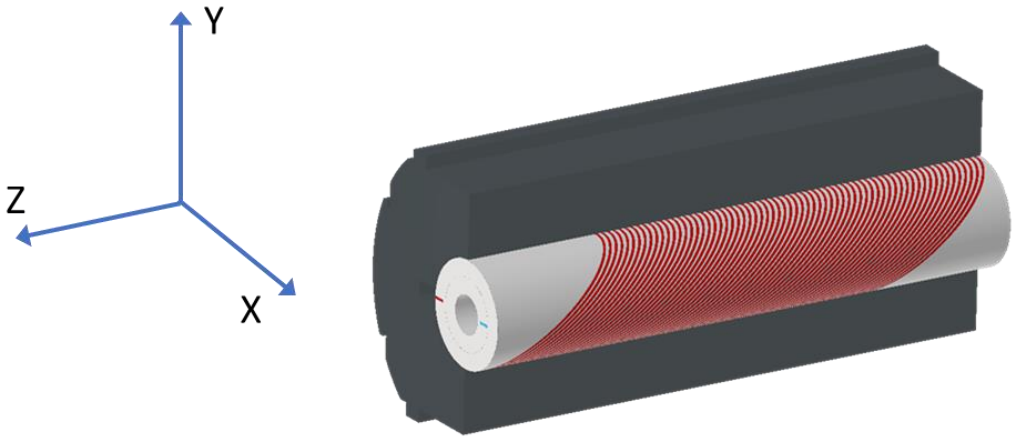

Figure 4. Coordinates reference system and 3D view of the CCT magnet assembly.

The former is a hollow cylinder (or toroidal sector in case of CCT curved) which contains a groove, obtained by machining, where the conductor is placed (Fig. 4). Moreover, the mandrel is characterized by ribs and spar. The ribs are thin wall between two consecutive turns of the groove while the spar is a thick wall between the hollow of the cylinder and the ribs (Fig. 5).

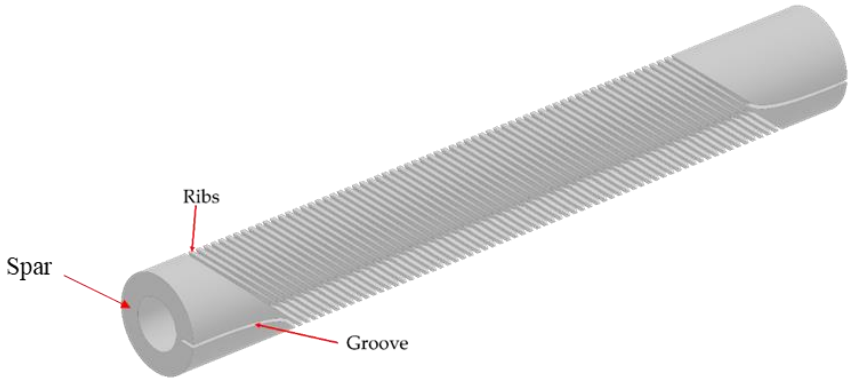

Figure 5. CCT former picture highlighting the ribs, groove and spar.

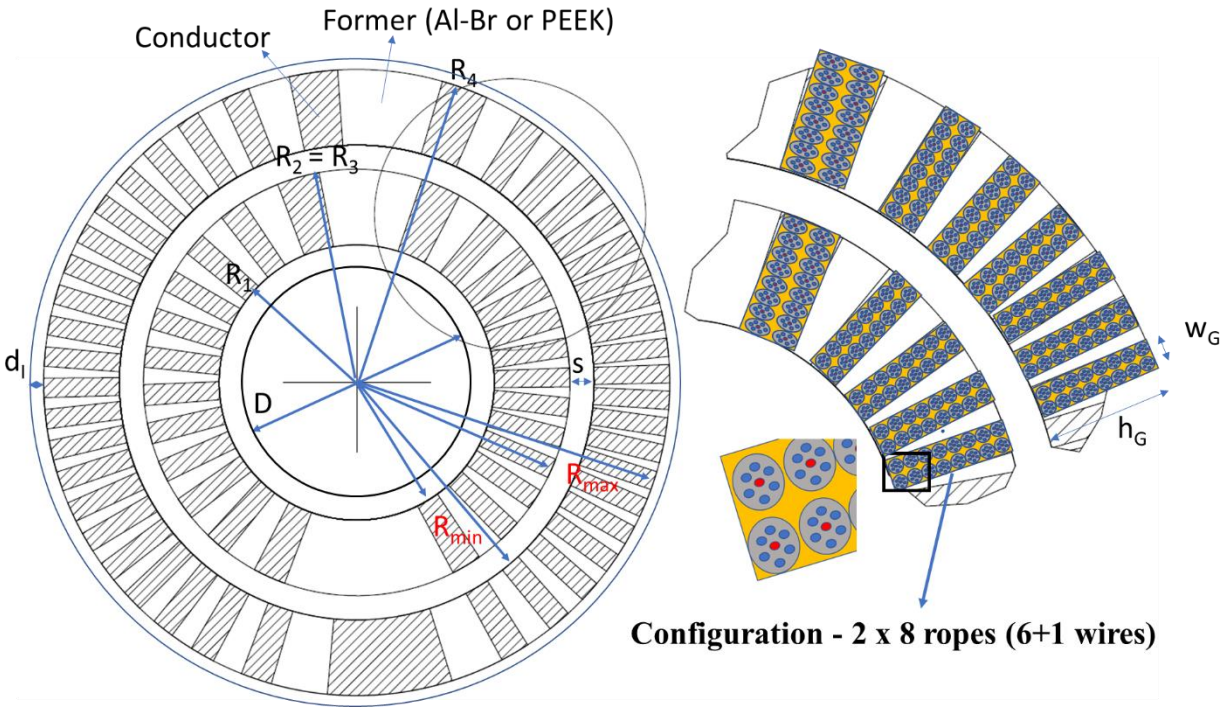

Figure 6. Cross section and some parameters of the two layers CCT formers (see Tab.4).

The figure 6 highlights some parameters of the CCT magnet presented, and it shows a representation of the cables (rope 6+1 wires, see previous paragraph) into the grooves. The table 4 reports the geometrical parameters used for the demonstrator (former and conductor radii, spar, groove and minimum ribs thickness, etc…), the number of turns and of ropes per groove. The distance between iron and former is fixed approximately at 2 mm (average value), as average value used for the magnetic design simulation. Indeed, the real distance will be not uniform (as reported in the mechanical section) due to different eccentricity between the former and the iron. The radial thickness of the iron yoke has been fixed at 100 mm (Tab.4, R_{outer} - R_{inner}) in order to have a minimum external field of 0.5 mT at about 2 meters from the magnet.

Table 4. CCT geometrical parameters: inner and outer layers

Parameters	**Values**		**unit**
	Inner	**outer**	
Bore diameter D	80		mm
Pitch	16.61		mm
Groove width w_G	5.7 (2.85 mm x 2)		mm
Groove height h_G	22.8		mm
Minimum ribs thickness	0.8		mm
Spar s	8		mm
R_1-R_3 (former)	40	70.8	mm
R_2-R_4 (former)	70.8	101.6	mm
R_{min} (conductor)	48	78.8	mm
R_{max} (conductor)	70.8	101.6	mm
Number of ropes per groove	16		-
Number of turns per layer	42		-
Iron – former distance d_I	2		mm
R inner - Iron	103.6		mm
R outer - Iron	203.6		mm
Max external field at 2 m	0.5		mT
Former material	Aluminum-Bronze, and PEEK		-

3. Magnetic design and field quality

The magnetic design of the combined function CCT demonstrator is presented in a 3D geometry following the CCT geometrical nature (double tilted solenoid) [11]. The simulation of the 3D model has been implemented in OPERA [13]. The CCT magnet model has been based on the parameters presented in the previous paragraphs (2.1, 2.2, 2.3 and 2.4). The magnet is designed to reach a bore field of 4 T by two layers of 16 twisted rope cable (6+1) winded around two formers, inner and outer ones (Fig. 4 and Tab. 4). The simulation results are divided in two subsections: one dedicated to the 3D magnetic design and the other one describing the field quality.

3.1 3D MAGNETIC DESIGN

The magnetic model implemented by OPERA is represented in the Fig. 7, where is highlighted the geometry of the conductor (in red) and the iron yoke (in green). The geometry is based on the parameters reported in Tab. 4 (section 2.4). The yoke geometry is designed in order to have a triple effect. The first one is to use the yoke as a collar, which allows to give pre-stress to the formers after the cooldown and to compensate the deformation due to the magnet energization (see the section 4, Mechanical design). The second one is to contribute together with the conductor to the main field target (bore field of 4 T). The third one is to shield the magnetic field in order to limit the external magnetic field at 0.5 mT (2 meters of distance from the yoke).

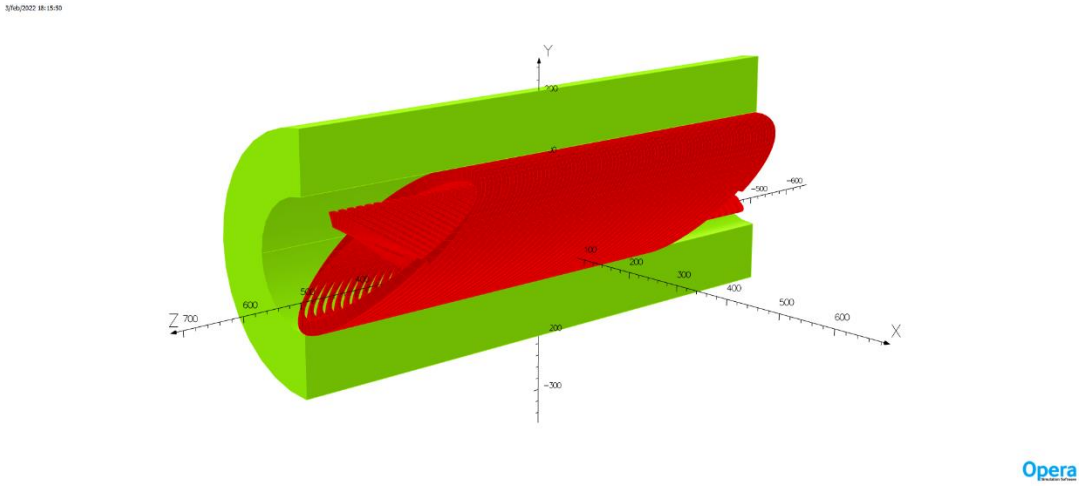

Figure 7. 3D magnetic model of the combined straight CCT demonstrator implemented by OPERA.

Table 5. Magnet performance

Operational temperature [K]	Short sample field [T]	Short sample current [A]
4.2	6.58	1968
4.7	6.15	1842

The CCT demonstrator in NbTi will be tested in He gas at 4.7 K (conduction cooled), but a preliminary test at 4.2 K may be performed at the INFN Laboratory of Accelerator and Applied Superconductivity (LASA). The outer diameter of the yoke is set to 407 mm, to have the possibility to accommodate the magnet in the cryostat of the LASA laboratory test station. The operational

current is 1308 A and the nominal bore field is 4.09 T (Tab. 7). The short sample values, 1842 A @ 6.15 T and 4.7 K, are reported in Table 5 and shown in Fig. 8. The load line is computed on the basis of the Jc dependence on magnetic field and temperature proposed by L. Bottura [14]:

$$J_c/J_c(4.2\ K@5T) = \frac{C_0}{B} b^{\alpha}(1-b)^{\beta}(1-t^n)^{\gamma} \qquad (1)$$

where $t = \frac{T}{T_{c0}}$ is the reduced temperature, $b = \frac{B}{B_{c2}(T)}$ is the reduced field, and the critical field dependence on temperature is taken from Lubell [15], $B_{c2} = B_{c20}(1-t^n)$, where n =1.7 provides a satisfactory fit. The equation (1) has 4 free parameters (see Tab. 6), a normalization constant C_0, two parameters describing the dependence on the reduced field, α and β, and a parameter describing the dependence on the reduced temperature, γ.

Table 6. Critical current density Jc – fit coefficients

C_0	α	β	γ	T_{c0}	B_{c20}	n
30.4032 T	0.833	1.167	1.398	9 K	14.5 T	1.7

As shown in the Fig. 8, the load line margin at the nominal current and at 4.7 K of operational temperature is of 28.7% and 33.4% at 4.2 K (liquid helium).

Table 7. Magnet performance parameters at nominal current.

Parameters	**values**	**units**
Nominal current (Rope)	1308	A
Bore field	4.09	T
Superconductor current density	953.4	A/mm^2
Copper current density	544.5	A/mm^2
Peak field	4.38	T
Operating temperature	4.7	K
Margin on loadline	28.7	%
Temperature margin	1.6	K
Stored energy	88.513	kJ
Static inductance	103.4	mH

Seeing the cross-section map of the magnetic field B (Fig. 9, left), the level of iron saturation is very high (more than 2 T). The field profile of B_y (Fig. 9, right) at the centre shows a smooth trend at the ends, as foreseen by the presence of iron. Fig. 9 shows also the homogeneous field region of 200 mm at 0.1% of homogeneity ($\Delta B/B_y(0,0,0) = 0.1\%$).

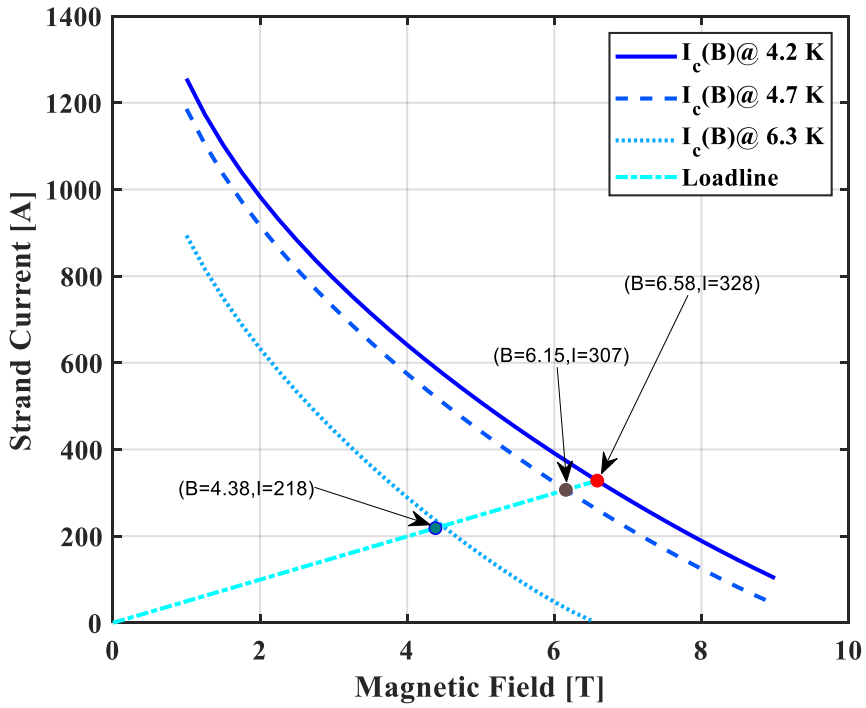

Figure 8. Peak field load-line at 4.7 K and 4.2 K. The margin on the load-line at nominal bore field is 28.7% at 4.7 K and 33.4 % at 4.2 K. The critical temperature curve is reported at 6.3 K (temperature margin of about 1.6 K).

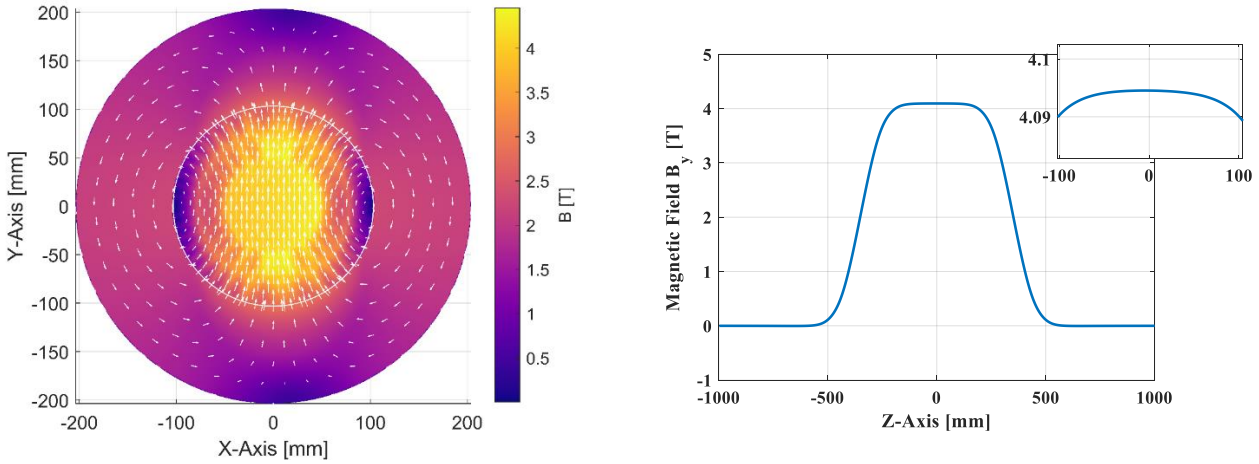

Figure 9. Magnetic Field map in the cross section and profile of B_y at center along z-axis. The zoom highlights the homogeneous field region of the B_y (200 mm at 0.1% of homogeneity).

The critical temperature is 6.3 K giving a temperature margin of about 1.6 K, as shown in figure 8. The peak field on the conductor is 4.38 T, giving a $B_{peak}/B_0 = 1.07$. In order to have a fringe field below the safety threshold of 0.5 mT (D.lgs. 81/08) [16] the clearance should be larger than 2 m. The magnetic length is of about 0.73 m, less than target one (0.8 m, Tab.1), but a good compromise by limiting the total length of the magnet to 1 m, i.e. to reduce costs. The figure 10 shows the magnetic field on the conductor, highlighting the distribution of maximum (red) and minimum (blue) field regions.

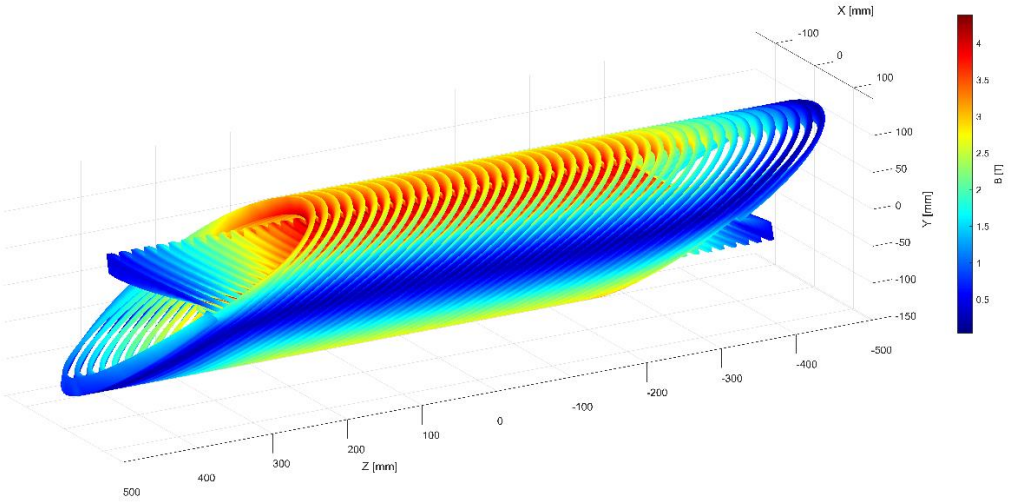

Figure 10. Magnetic field on the conductor of the CCT.

3.2 FIELD QUALITY

The field quality is computed with OPERA assuming the two-dimensional multipolar expansion in European notation [17]:

$$B_y(x,y) + iB_x(x,y) = 10^{-4}B_0 \sum_{i=1}^{+\infty} (b_n + ia_n) \frac{(x+iy)^{n-1}}{R_{ref}^{n-1}}$$

The reference radius R_{ref} is defined to be 26.67 mm, i.e. 2/3 of the magnet aperture radius of 40 mm. The expansion is valid locally, i.e. in the bore field aperture, where B_0 is the main harmonic component (dipole value in our case), b_1 = 10^4, and the other normal b_n and skew a_n normalized harmonics are measured in 'units' ($10^{-4}B_0$). As shown in Tab. 8, the magnet presents a quadrupole of about 325 units, corresponding to the 5 T/m of quadrupole combined to the dipole. The skew harmonics are all zero for the design symmetry. As reported in Fig. 11, the longitudinal profile of the harmonics A_n is symmetric and cancel out on the field integral. The presence of 6.3 units of b3 means that the magnetic design could be improved. At this stage, the requirement is not stringent for the harmonics because the field quality is a secondary target with respect to the nominal field.

Table 8. Field quality at nominal current and reference radius 26.667 mm.

Parameters	Values	units
Operational current	1308	A
Reference radius	26.667	mm
b2	325,40	10^{-4}
b3	6,80	10^{-4}
b5	0,90	10^{-4}
b6	0,00	10^{-4}
b7	0,00	10^{-4}
b9	0,61	10^{-4}
b10	0,05	10^{-4}

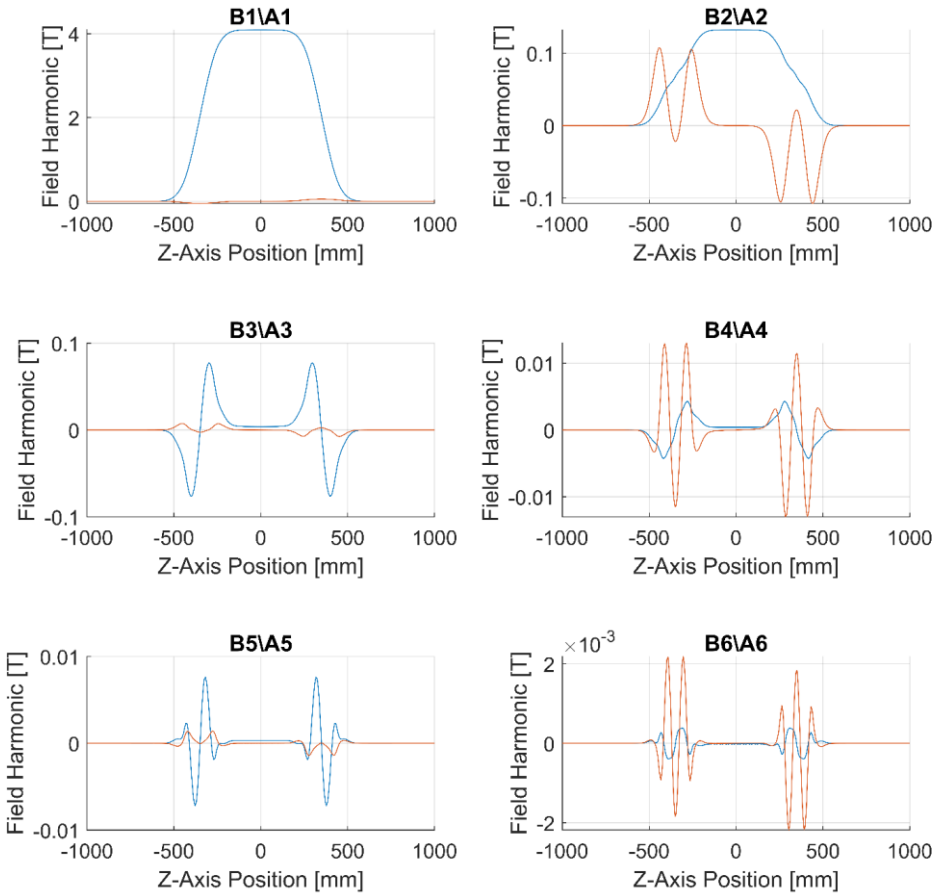

Figure 11. Non-normalized normal and skew field harmonics profile along the longitudinal z-axis.

4. Mechanical design

After the electromagnetic study the mechanics of the magnet has been investigated. This section explains the mechanical structure evaluated to contain the ovalization of magnet (see paragraph

4.2.3), the finite element model (FEM) simulated with ANSYS, the investigated materials and the results of the simulations.

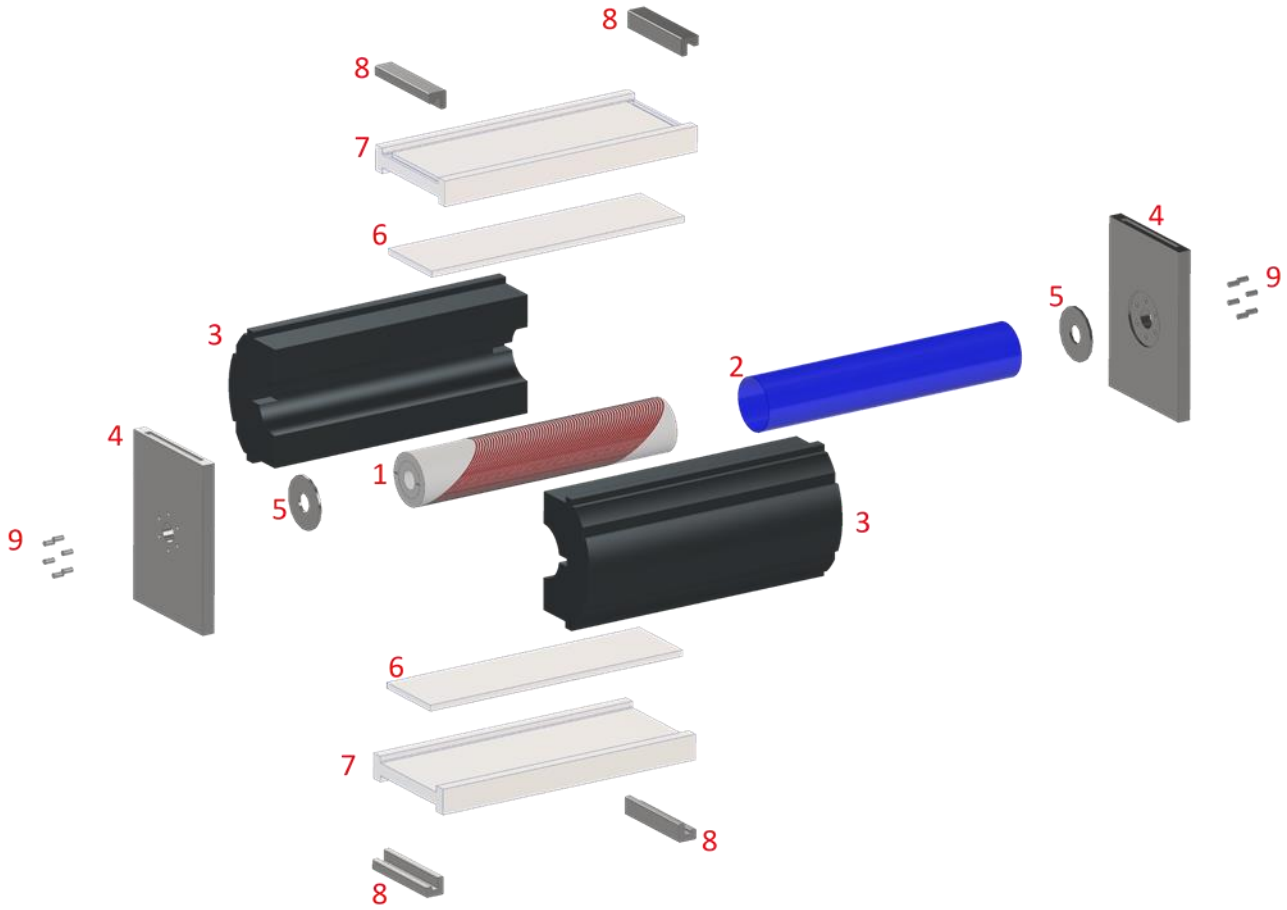

Figure 12. Exploded view of the mechanical structure, elements are reported in the subsection 4.1.

4.1 DESCRIPTION OF THE MECHANICAL STRUCTURE

The main mechanical components of the magnet are presented, as reported in Fig. 12:

1) Two layers CCT magnet (see previous sections, 2.4).
2) Thin layer (0.5 mm thick) made of G10 which covers the CCT. This layer must insulate and protect the conductor.
3) Iron yoke is divided in two halves that must remain attached to the CCT to contain the ovalization given by Lorentz forces. The halves of iron are not concentric with the CCT (the centres of the circumferences are 1 mm distant) to have contact just on the midplane of the structure (see Fig. 13).
   The two halves are separated by a gap, not constant, opened at room temperature and closed at 4.2 K.

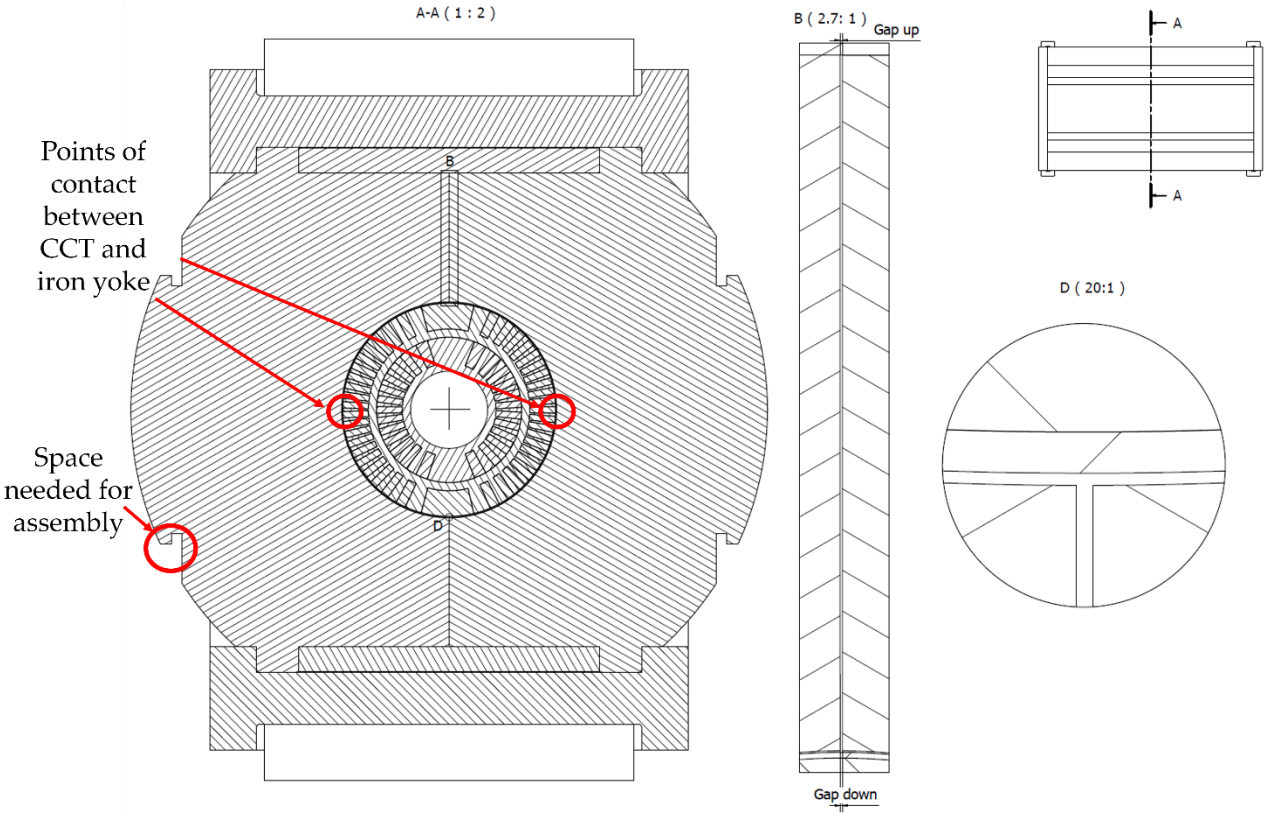

Figure 13. Cross section (A-A) of the mechanical structure. In the detail B, the gap between the two parts of iron is highlighted, the gap which is not constant (at the bottom is smaller than at the top as shown in Table 1). In the detail D, we can see the small space between the iron and the CCT.

The bigger the gap between iron halves at room temperature the higher the contact between the CCT and iron when the magnet is energised, but the risk of not closing the gap between the two parts of iron at cryogenic temperature is higher. So, the value of the gap of iron is a trade-off between the contact of iron and CCT and the contact between iron halves.

In order to find the optimal value of the gap between the halves of iron yoke, different simulations have been performed. In this case a full 3D simulation has high computational cost due to the large number of components and nonlinear (frictional) contacts. For this reason, 2D simulations have been done first to obtain a quick indication of the right value of the gap, then full 3D simulations have been performed to obtain more reliable values. The table 9 shows the optimal values of gap achieved.

Table 9. Values of the gap between the iron halves (room temperature).

Material	Gap up [mm]	Gap down [mm]
PEEK GF30	0.40	0.38
Aluminium Bronze 954	0.42	0.40

4) At the extremities of the structure there are two end plates (made of AISI 316L), containing six preloaded bolt which press on the CCT to contrast the action of Lorentz forces at magnet extremities which tend elongate the CCT.
5) At the extremities of the magnet there are two small plates made of AISI 316L which must distribute uniformly the action of bolts on the CCT. The small plates are attached to the magnet with glue which can fill eventual empty spaces between the magnet and the small plate thus maximising distribution of bolt's forces on the CCT.
6) Two mechanical stoppers are present to assure the alignment of the two iron halves with the open gap during the assembly process. The stoppers must contract as much as the clamps at least, because this allows to the stoppers to shrink more than clamps and iron during cool and so do not interfere with the rest of the structure. The material selected for the stoppers is aluminium 6082-T6.
7) Two clamps are present at the top and bottom of the structure. The clamps must be made of a material which contracts more than the CCT formers and iron yoke to keep the two iron halves attached to the magnet. In fact, all the possible materials for the formers contract more than iron and this leads to detachment during cool down. The material selected for the clamps is aluminium 6082-T6 due to its high thermal contraction.
8) There are four joints with 'c' shape which connects the end plates to the rest of the structure.
9) Bolts preloaded to contrast the action of Lorentz forces.

4.2 MECHANICAL SIMULATIONS

The loads of the mechanical simulations have been applied in three sequential steps: 1) bolts preload, 2) cooldown and 3) energization. The model used for mechanical simulations (with ANSYS Workbench) is one quarter of the whole mechanical structure (Fig.14). The energization used the Lorentz forces imported by COMSOL (Fig.15).

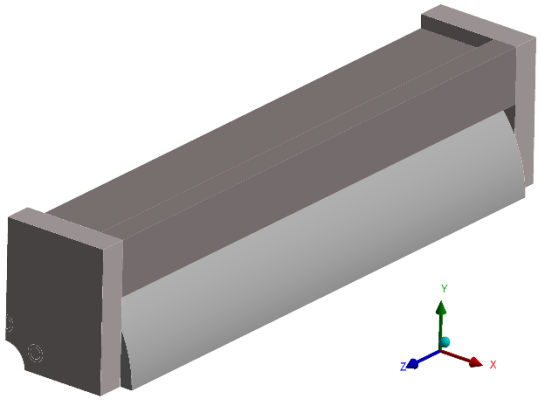

Figure 14. ANSYS model: one quarter of the structure shown in the Fig.2.

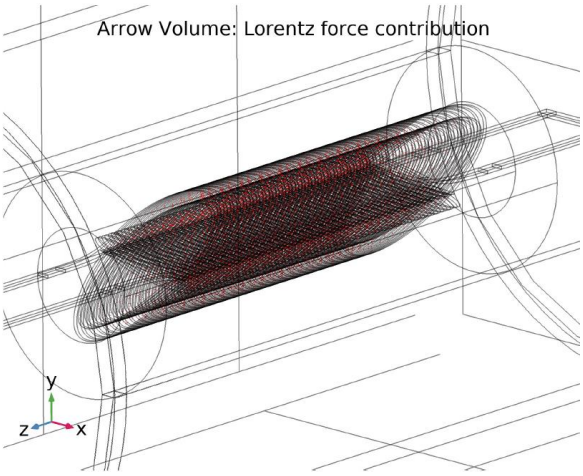

Figure 15. Lorentz forces evaluated by COMSOL.

This can be done due to the symmetry of electromagnetic forces which were evaluated dividing the CCT into four quadrants along the longitudinal direction (evaluation done by COMSOL), as shown in the Fig. 16.

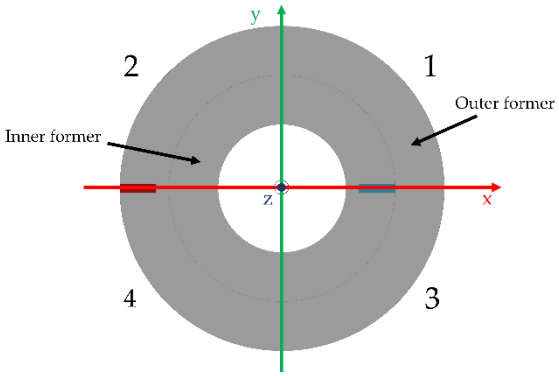

Figure 16. CCT quadrant division.

Table 10. Lorentz forces in the four quadrants.

Forces	Quadrant 1	Quadrant 2	Quadrant 3	Quadrant 4
F_x [N]	4.69e5	-4.45e5	4.69e5	-4.45e5
F_y [N]	-1.25e5	-75639	1.25e5	75637
F_z [N]	-40763	-31331	40762	31328

As reported in Tab.10, the forces are well symmetric with respect to the XZ plane. Forces are symmetric also with respect YZ plane except for F_x, but the difference found is just of 5%. Hence, the model was also considered symmetrical with respect to the YZ plane.

4.2.1 Constraints:

One extremity of the magnet is constraint not to move along the Z axis (Fig.17).

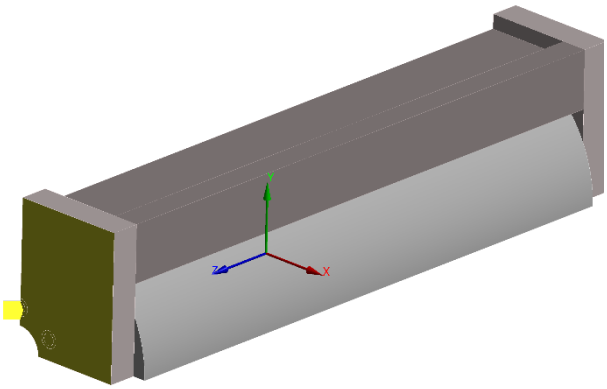

Figure 17. Faces constraint not to move along Z (yellow faces).

In order to define the condition of symmetry of one quarter of the magnet, all the faces on the YZ plane cannot move along X and each face on the XZ plane cannot move along Y (Figs.18 and 19).

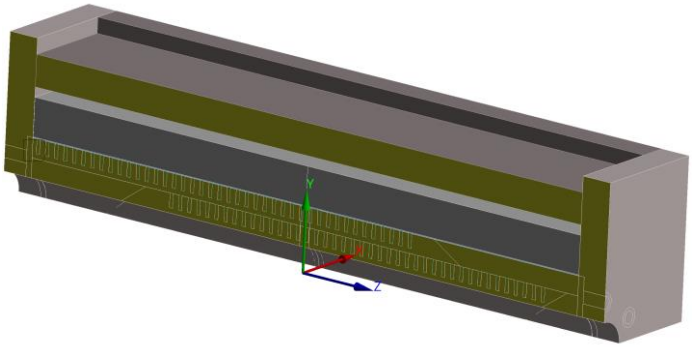

Figure 18. Faces constraint not to move along X (yellow faces).

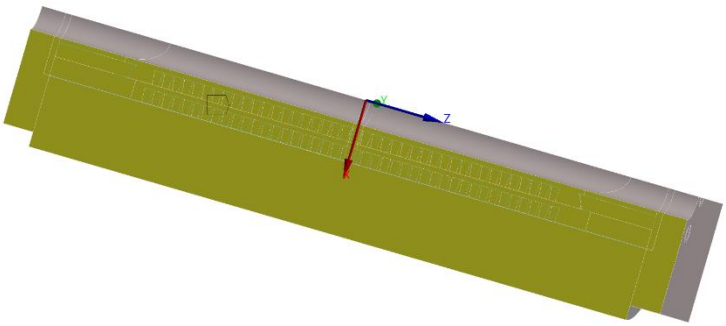

Figure 19. Faces constraint not to move along Y (yellow faces).

4.2.2 Materials

The materials simulated for the former are aluminium bronze 954 [18] and PEEK GF30 [19,20] (polyether-ether-ketone reinforced with 30% of glass fibres), mechanical properties reported in Tab.11. Aluminium bronze has high rigidity and it is easy to machine with respect to stainless steel and titanium. Moreover, first calculations of eddy current losses show that aluminium bronze may be suitable (see section 6). PEEK GF30 is plastic, so it eliminates the problem of eddy currents and it has good mechanical properties with respect to other plastics [19, 20]. Moreover, short glass fibres are oriented in a casual way in the material, so its behaviour is almost isotropic.

Table 11. Former's materials properties.

Material	Temperature T [K]	Young Modulus E [GPa]	Poisson Ratio ν [-]	Tensile Limit [MPa]	Coefficient of thermal contraction $\alpha_{293K-4.2K}$ [1/K]	Refs
PEEK GF30	293	11.6	0.39	200 (ultimate strength)	10.4e-6	[19, 20]
	4.2	18.1	0.39			
Aluminium Bronze 954	293	110	0.316	640 (yield strength)	10.8e-6	[18]
	4.2	114.4	0.316			

The conductor of Nb-Ti has been modelled as a homogenised orthotropic material [18](Tabs.12 and 13), whose properties are referred to the local reference system of the winding path (see Figs. 20 and 21). Moreover, a homogenisation technique was used to obtain realistic coil properties to account for both the Nb-Ti strands and the cured resin [18].

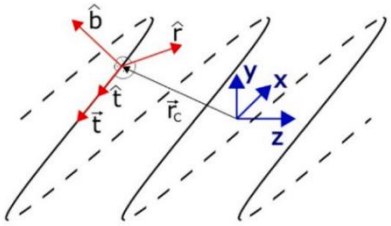

Figure 20. Local reference system of the winding path (Fig. from [3] - courtesy of Glyn Kirby).

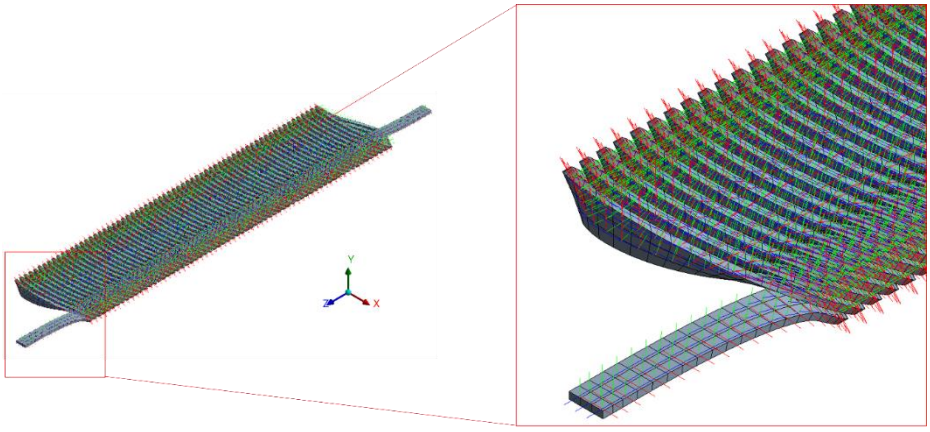

Figure 21. Local reference system of the elements of the conductor.

Table 12. Mechanical properties of the coil along the radial, binormal and tangential directions (E-Young modulus, ν-Poisson ratio and G-Shear modulus).

T	E_r	E_b	E_t	ν_{rb}	ν_{bt}	ν_{rt}	G_{rb}	G_{bt}	G_{rt}

[K]	[GPa]	[GPa]	[GPa]	[-]	[-]	[-]	[GPa]	[GPa]	[GPa]
293	11.9	11.9	59.0	0.36	0.07	0.07	2.57	3.45	3.45
4.2	25.8	25.8	61.2	0.38	0.16	0.17	5.7	7.27	7.27

Table 13. Coefficients of thermal contraction of the coil in the local reference system.

$\alpha_{r_293K-4.2K}$ [1/K]	$\alpha_{b_293K-4.2K}$ [1/K]	$\alpha_{t_293K-4.2K}$ [1/K]
23.9e-6	23.9e-6	9.85e-6

4.2.3 Simulations Results

We report simulations results in terms of stress, radial and azimuthal displacements. The results show no criticalities from the mechanical point of view. The stresses on the formers are well below the limit of both materials. The highest magnitude of the stresses is due to compression (in the minimum principal stress, Figs 22.c and 23.c), for both materials. Assuming the behaviour of the materials at compression symmetric with respect to traction, the minimum safety factor is 1.67 for PEEK GF 30 and 2.37 for aluminium bronze 954.

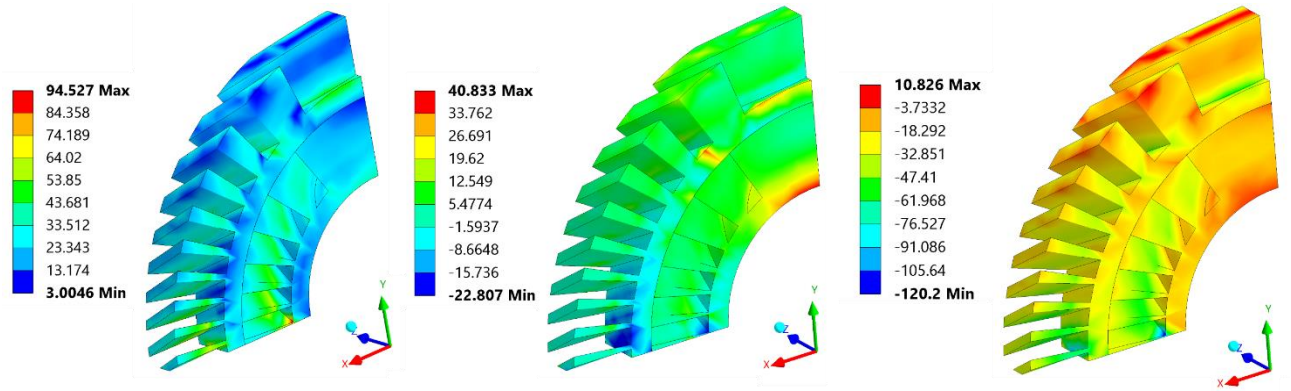

(a) (b) (c)

Figure 22. Von Mises (a), Maximum Principal (b) and Minimum Principal (c) stresses, after the cool down and the energization of the CCT, expressed in MPa in the formers made of PEEK GF30.

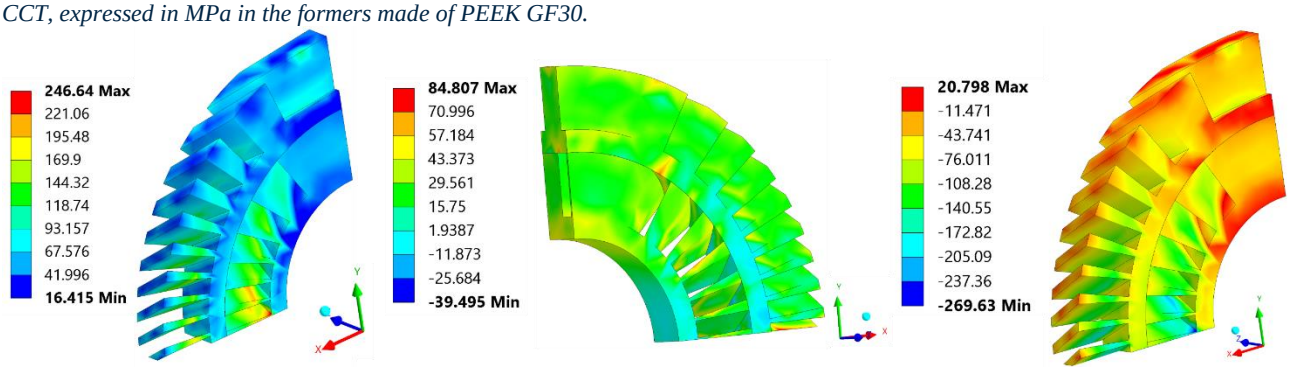

(a) (b) (c)

Figure 23. Von Mises (a), Maximum Principal (b) and Minimum Principal (c) stresses, after the cool down and the energization of the CCT, expressed in MPa in the formers made of aluminium bronze.

In case of both materials, the stresses on the conductor are far from the yield limit of 300 MPa [18] of Nb-Ti. The longitudinal strain of the NbTi strand is not impacting on the critical current. The

highest magnitude of the stresses is due to traction (in the maximum principal stress, Figs 24.b and 25.b), for both materials. Hence, the minimum safety factor is 2.45 for PEEK GF 30 and 3.48 for aluminium bronze 954, but it is important to remember that these stresses are just an indication. Indeed, the coil is modelled just as an orthotropic material and the real structure and single strands which compose the conductor are not present in the FEM model.

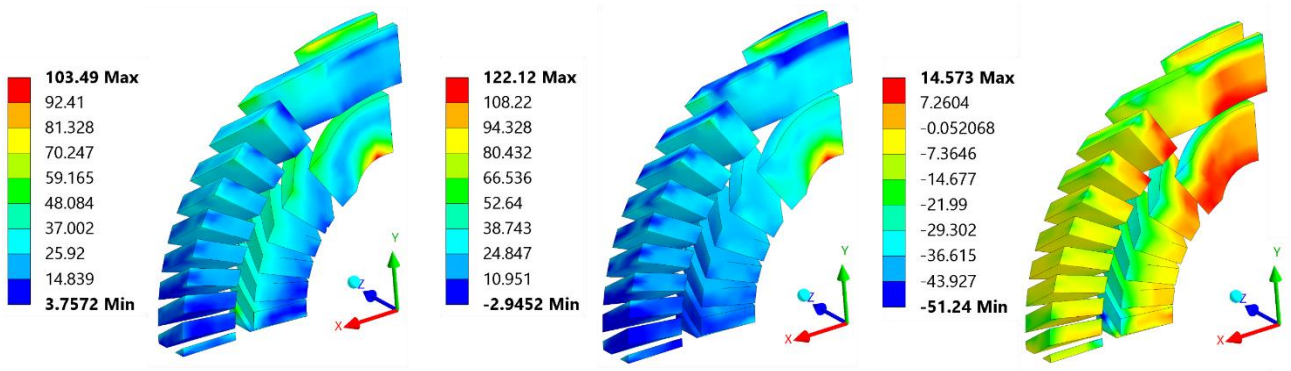

Figure 24. Von Mises (a), Maximum Principal (b) and Minimum Principal (c) stresses in the conductor, after the cool down and the energization of the CCT, expressed in MPa in case of formers made of PEEK GF30.

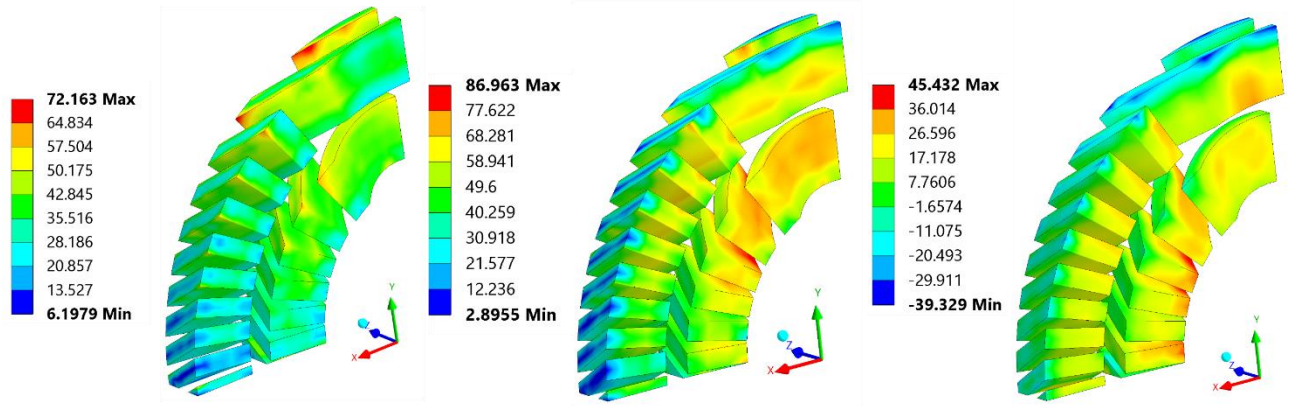

Figure 25. Von Mises (a), Maximum Principal (b) and Minimum Principal (c) stresses in the conductor, after the cool down and the energization of the CCT, expressed in MPa in case of formers made of aluminium bronze 954.

Radial displacements have been calculated to verify that the magnet remains circular since this is necessary to keep good field quality. At this preliminary stage, the thermal contraction makes the magnet smaller but does not affect the circular shape, so the figure of merit to evaluate the circularity of the CCT is the difference of radial displacement between the application of Lorentz forces and the cool down, which indicates the ovalization of the magnet. If the magnet remains circular, this difference must remain within a certain limit for points which lay on the same radius (Fig. 26).

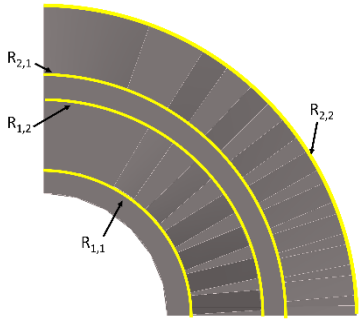

Figure 26. Radii where the difference of radial displacements were evaluated.

The Figures 27 and 28 show the differences of radial displacements between energization and cooldown for the radii shown in Fig. 26.

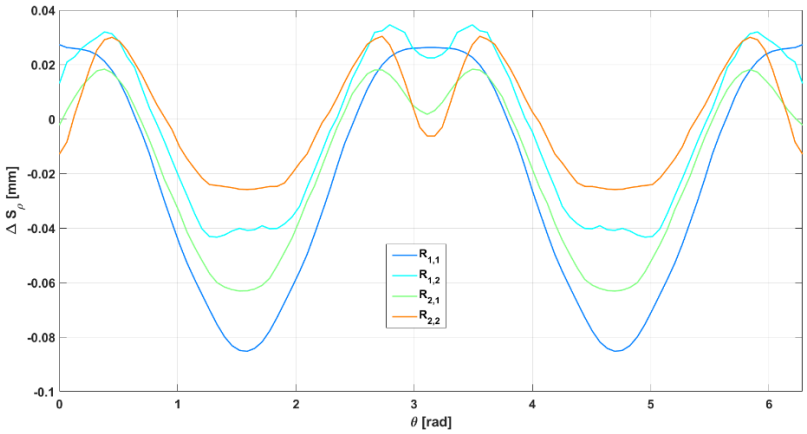

Figure 27. Difference of radial displacements between the application of Lorentz forces and the cool down process for the points which lay on $R_{1,1}$, $R_{1,2}$, $R_{2,1}$ and $R_{2,2}$. The graph refers to PEEK GF30.

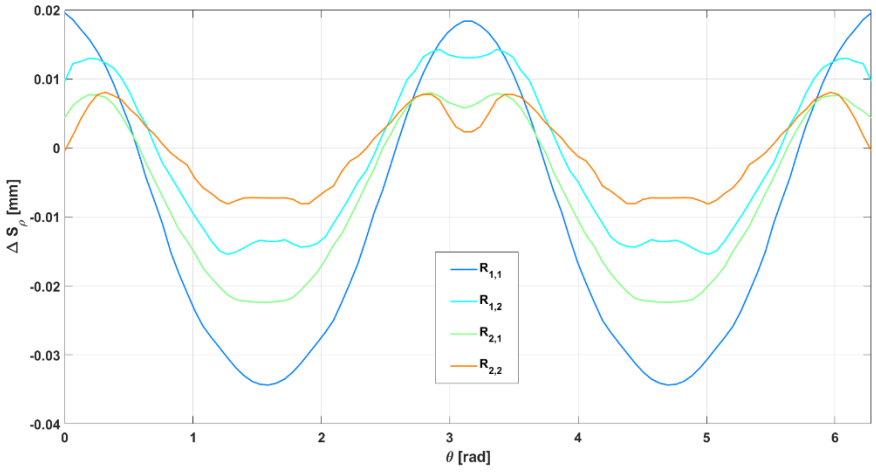

Figure 28. Difference of radial displacements between the application of Lorentz forces and the cool down process for the points which lay on $R_{1,1}$, $R_{1,2}$, $R_{2,1}$ and $R_{2,2}$. The graph refers to aluminium bronze 954.

The Table 14 shows the maximum deviation of the curves in Fig. 27 and Fig. 28.

Table 14. Maximum deviation of radial displacement at different radii.

	$R_{1,1}$	$R_{1,2}$	$R_{2,1}$	$R_{2,2}$

Maximum deviation for PEEK GF 30 [mm]	0.1138	0.0907	0.0858	0.0605
Maximum deviation for aluminium bronze 954 [mm]	0.05427	0.03467	0.03195	0.02023

To maintain the magnet circular the differences shown in Table 14 must be monitored. In case of aluminium bronze 954, the differences are of the order of 10 µm, while for PEEK GF30 the differences are of about 100 µm which may be critical.

Azimuthal displacements have been evaluated but they remain well below the 100 µm (Fig.29) and they are less critical with respect to radial ones. Despite this, it is important to notice that the imposed symmetry conditions give huge contribution to keep azimuthal displacements low. Hence, to have a more accurate evaluation of azimuthal displacements, another simulation should be implemented to consider a real system of keys (such as the ones in Fig. 30).

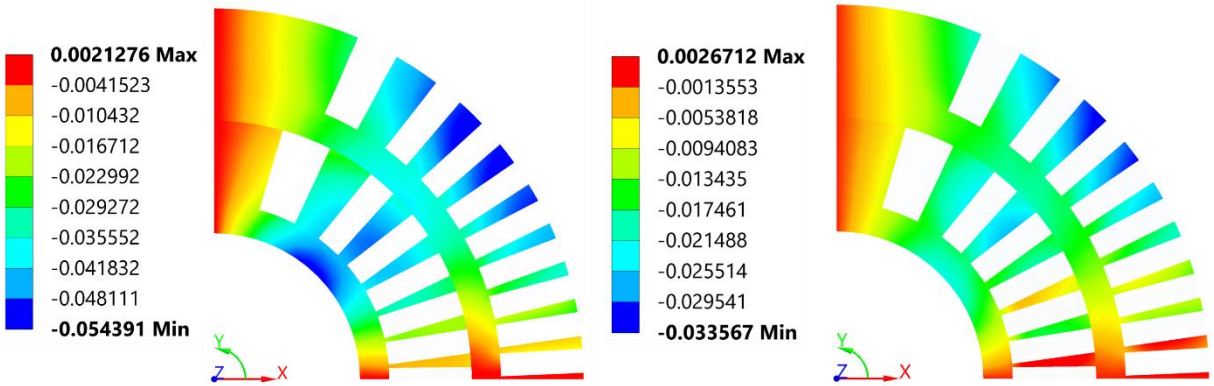

(a) b)

Figure 29. Azimuthal deformations, expressed in mm, after the cool down and the energization of the CCT for PEEK GF30 (a) and aluminium bronze 954 (b).

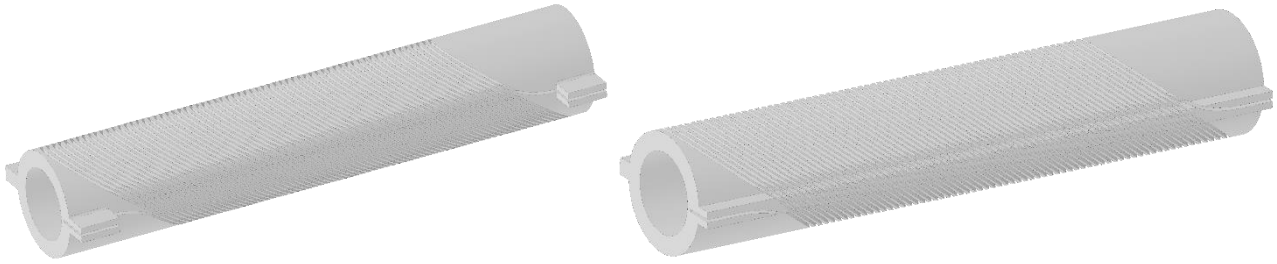

(a) (b)

Figure 30. Two possible system of keys for the alignment of the magnet. The case (b) is closer to the constraints imposed in FEM simulations.

5. Stability and protection

The following section is focused on the protection limits of the combined CCT demonstrator presented. The main idea is to give an overview of the protection parameters of the magnet, and verifying if the rope cable with a copper core is suitable from the protection point of view.

The electrical scheme of the magnet protection is presented in Fig. 31. It includes the two layers windings that form the CCT magnet, the dump resistor, the power supply and the main switch. The circuit is grounded at one terminal of the power supply.

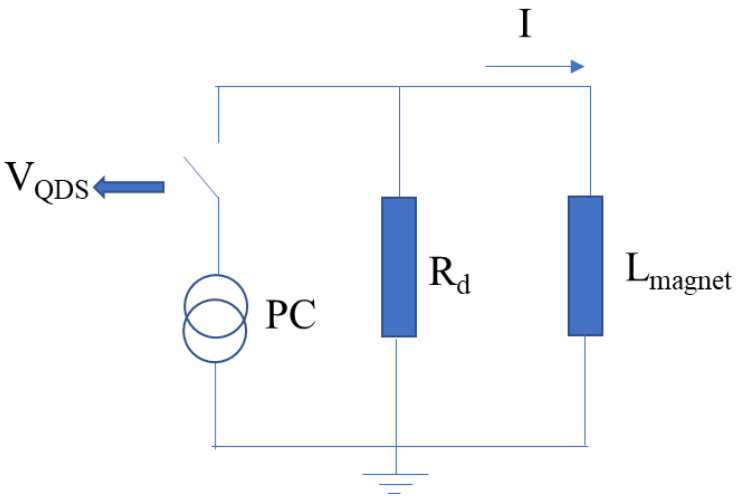

Figure 31. Electrical scheme for magnet protection.

Table 15 reports some of the main parameters for the protection study of the rope 6 NbTi +1 copper core strands (nominal configuration), and of the rope with 7 NbTi strands. The magnetic stored energy was evaluated by COMSOL and crosschecked analytically. The inductance has been derived from the energy (2) neglecting the effect of the iron yoke, and the dumping resistor from the maximum voltage set to 300 V (3).

$$L = \frac{2U}{I_o^2} \tag{2}$$

$$R_d < \frac{V_{max}}{I_0} \tag{3}$$

where I_0 is the nominal current and U is the magnetic stored energy. Assuming negligible the resistance built up in the magnet during the quench, the current decay in the circuit of Fig. 31 [21] follows (4):

$$I(t) = I_0 exp\left(-\frac{tR_d}{L}\right) \tag{4}$$

From (4), the quench integral is evaluated as:

$$\Gamma_q = \int_0^\infty I^2(t)dt = I_0^2 \int_0^\infty exp\left(-\frac{2tR_d}{L}\right) dt = \frac{LI_0^2}{2R_d} \tag{5}$$

and reported in Tab. 15.

Table 15. Main parameters for the protection study: rope (6 NbTi strands+1 copper core strand) and rope (7 NbTi strands) .

Parameters	**Values**		**units**
	Rope (6 NbTi +1 Cu)	**Rope (7 NbTi)**	
Nominal current I_0	1308	1494	A
Inductance L	103.4	79.3	mH
Magnetic stored energy U	88.513		kJ
Dumping resistance R_d	0.230	0.200	Ω
Time constant (L/R_d)	0.451	0.395	s
Maximum voltage V_{max}	300		V
Quench integral Γ_q	0.386	0.441	MA^2s
Fraction of superc. k_{sc}	0.363	0.424	-
Fraction of copper k_{Cu}	0.466	0.376	-
Fraction of CuMn k_{CuMn}	0.171	0.200	-
Rope surface A	3.706		mm^2
Integral Γ (T_{max} = 300 K)	0.942	0.774	MA^2s
Time margin t_q	0.325	0.149	s

Neglecting the time needed to detect the quench and insert the dump resistor, and following the adiabatic approximation, the condition of protection is:

$$\Gamma_q < \Gamma = A^2 \nu \int_{T_{op}}^{300} \frac{C_p(T)}{\rho_{Cu}(T)} dT = A^2 \nu \gamma^{300} \quad (6)$$

where A is the rope surface, ν is the fraction of Cu plus the fraction of CuMn in insulated cable and γ^{300} is the integral of the ratio between volumetric specific heat of the rope, C_p, and the copper resistivity, ρ_{Cu}, fixing the hotspot temperature to 300 K (safe temperature for the cable). In order to evaluate the upper limit of the protection condition, an estimate of the volumetric specific heat of the rope, C_p , has been done (Eq. 7), considering the superconductor, Cu and CuMn fractions of the two case studies (Tab. 15). The values of volumetric specific heats for the NbTi, Cu and CuMn, and the Cu and CuMn resistivities have been evaluated by the MATPRO program [22].

$$C_p(T) = k_{sc} * C_p^{NbTi}(T) + k_{Cu} * C_p^{Cu}(T) + K_{CuMn} * C_p^{CuMn}(T) \quad (7)$$

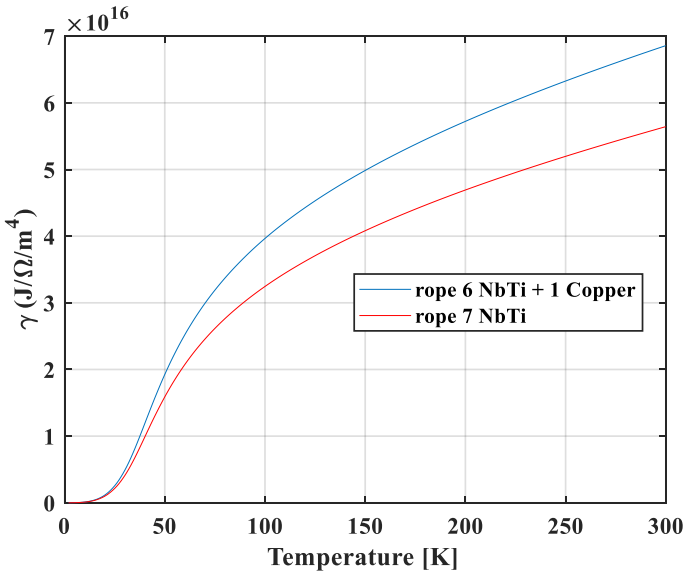

Figure 32. Integral of the ratio between volumetric specific heat of the cable and the copper resistivity for rope 6 NbTi + 1 copper strands (blue line), and 7 NbTi strands (red line).

As shown in the Fig. 32, the integral γ is less than a typical LHC NbTi cable with half of copper in the cross section, γ (T = 300 K) is about 10^{17} J/Ω/m^4, i.e. the rope cables presented have less fraction of copper in the cross section (Tab. 15). The equivalent MIIT curves are shown in Fig. 33, and highlighting the difference between the two ropes, the 6 NbTi +1 copper one has a 17% higher limit than the 7 NbTi strands one. The time margins for protection of the two rope solutions are evaluated by the following equation:

$$t_q = \frac{\Gamma(T_{max}) - \Gamma_q}{I_0^2} \tag{8}$$

As reported in the Tab. 15, the time margins are large compared to a high field magnet (100 ms for NbTi magnets, and 50 ms for Nb3Sn ones), and considering to protect the magnet with a traditional quench detection with intervention delays in the order of 50 -100 ms, the protection of this magnet could be easily setup. Fig. 34 shows the equivalent hotspot temperatures reached with 4 different delays of the quench detection, including the detection and validation time, and the opening of the main switch. The hotspot temperature for the rope 6 NbTi + 1 copper core strands could be reduced at 200 K with still a large margin for the protection. The rope 7 NbTi strands could be protected with a validation time of 100 ms.

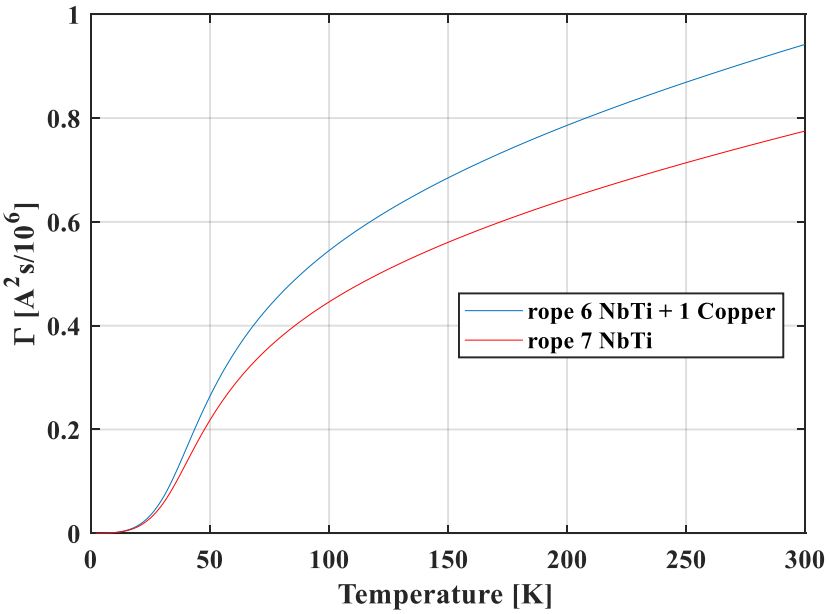

Figure 1. Integral Γ (or MIIT curve) calculated from T_{op} = 4.7 K up to T_{max} = 300 K.

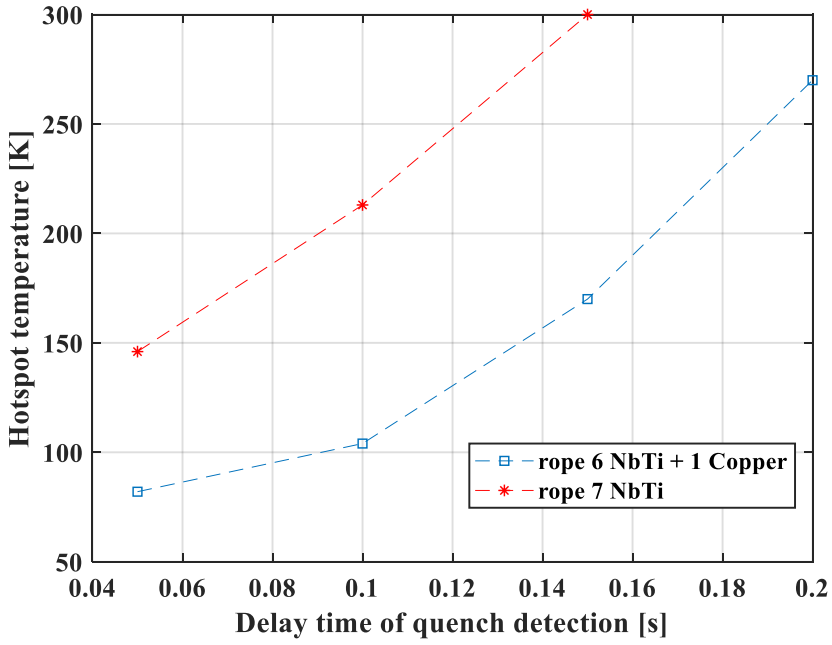

Figure 2. Hot spot temperature vs. the delay time of quench detection for rope 6 NbTi + 1 copper strands (blue line), and 7 NbTi strands (red line).

6. Power Losses

The section will present a preliminary study about the power losses of the combined CCT magnet. For a fast-ramped magnet, it is particularly critical to evaluate and control the power dissipated in the cold mass during the rapid cycle of the magnet. The main power losses sources are considered in the evaluation, focusing on the conductor and metallic former losses. At the end a focus on the current leads power consumption is presented in order to give a balance of the power needed.

6.1 Conductor Losses

The main dissipative sources for the conductor are the magnetic hysteresis in the superconductor and the interfilament coupling currents. In the following subsections, the persistent currents and interfilament coupling currents losses are presented and evaluated.

6.1.1 Persistent Currents Magnetization Loss

The main loss contribution for the conductor comes from the hysteretic losses within superconducting filaments, P_{PC}. This is function of the magnetization generated by the persistent currents, $M_{PC,}$ which, for the case of one round filament of diameter d_f and critical current $J_c(B)$(see paragraph 2.2), is

$$M_{PC} = \frac{2}{3\pi} d_f J_c(B) \left(1 - \left(\frac{J_t}{J_c(B)}\right)^2\right) f_{sc} f_{block} \qquad \text{[A/m]} \qquad (9)$$

where the f_{sc} is the fraction of superconductor in strand, f_{block} is the fraction of conductor with respect to the single block surface (see 2D model of Fig. 35), and J_t is the transport current density. The hysteretic power per unit volume due to the persistent currents is defined as the magnetization M_{PC} times the field derivative dB/dt:

$$p_{PC} = M_{PC} \frac{dB}{dt} = \frac{2}{3\pi} d_f J_c(B) \left(1 - \left(\frac{J_t}{J_c(B)}\right)^2\right) f_{sc} f_{block} \quad \text{[W/m}^3\text{]} \qquad (10)$$

where the dB/dt is the local field variation (0.4 T/s at center, as reported in the previous sections). The reduction of this kind of loss has been already considered during the manufacturing of the strand, originally done for the DISCORAP project [9]. Indeed, the filament diameter has been reduced down to 3.1 µm, and the wire presents a high purity Cu and Cu0.5wt%Mn matrix suppressing the proximity effect [9]. The complete problem of the field generated by the transport current has then been solved using COMSOL. The power density is a function of the local magnetic field on the conductor and for this it has been evaluated from the 2-D map of magnetic field calculated by COMSOL (Fig. 35).

Fig. 36 shows the magnetization map of the conductor due to the persistent currents and the associated power density at nominal field. As foreseen by theory, the power density changes during the ramp because the magnetization M_{PC} decreases as the field increases.

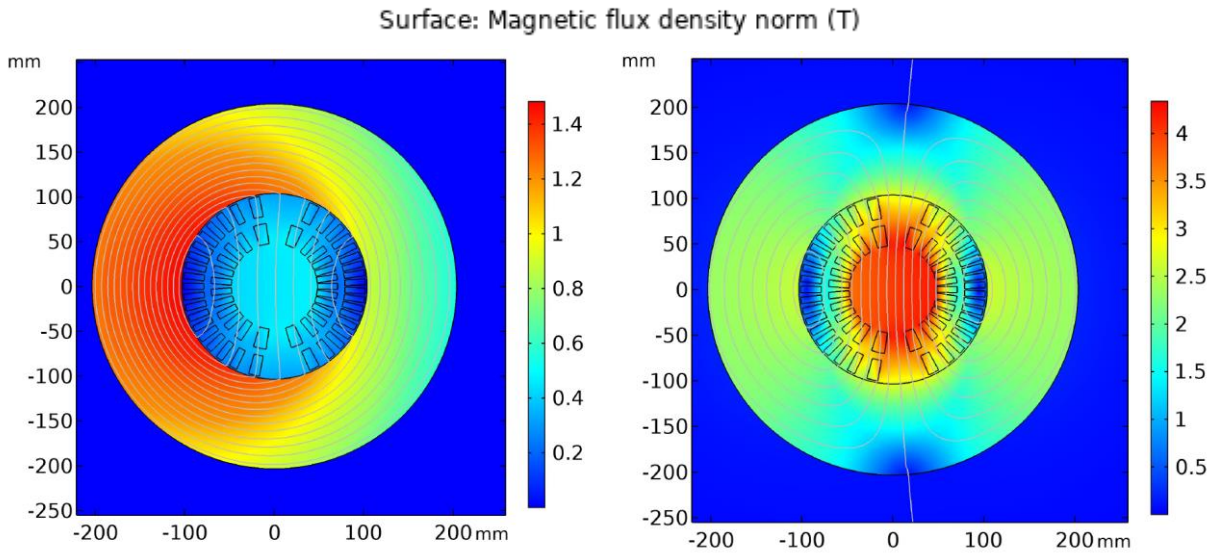

Figure 3. 2D CCT magnetic model: field map with a bore field of 0.45 T (left side), and 4.09 T (right side) at nominal current.

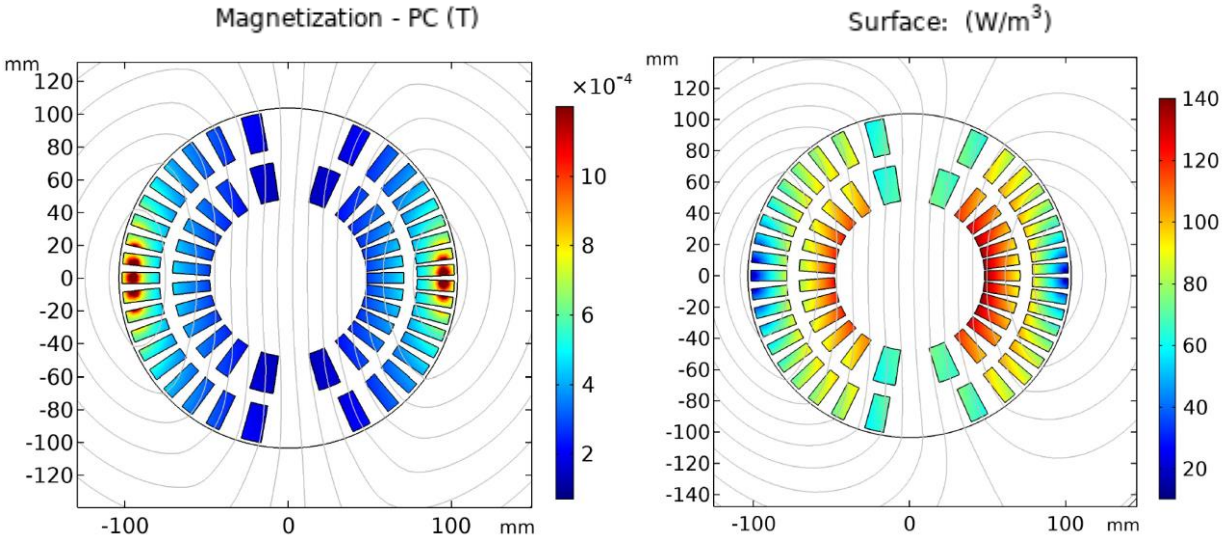

Figure 4. Magnetization M_{PC} and power density, $P_{PC,}$ maps generated by the persistent currents at nominal field, of 4 T.

6.1.2 Interfilament Coupling Currents Loss

The currents induced by a changing external magnetic field, normal to the wire axis, and dissipated in the resistive matrix by Joule effect, represent the second contribution of the conductor to the power losses. These currents are known as interfilament coupling currents, and they flow in loops composed by different superconducting filaments and closed through the matrix, in a plane normal to the wire axis [22]. The coupling magnetization is defined as

$$M_{IFCC} = -\frac{2}{\mu_0}\lambda_{fb}\frac{dB}{dt}\tau f_{cond} \qquad \text{[A/m]} \tag{11}$$

where the λ_{fb} is defined as d_{fb}^2/d_w^2 , as the filling factor of the filament region diameter, d_{fb} and the strand diameter, d_w; f_{cond} is the conductor surface fraction with respect to the single block surface, and τ is a time constant defined as

$$\tau = \frac{\mu_0}{2\rho_t}\left(\frac{p}{2\pi}\right)^2 \quad [s] \tag{12}$$

where p is the twist pitch of the filaments and ρ_t is the transverse resistivity across the copper matrix. The power per unit volume due to the interfilamentary currents is given by

$$p_{IFCC} = -M_{IFCC}\frac{dB}{dt} = \frac{1}{\rho_t}\left(\frac{dB}{dt}\right)^2\left(\frac{p}{2\pi}\right)^2 \quad [W/m^3/cycle] \tag{13}$$

In the evaluation, the transverse resistivity has been taken by the DISCORAP calculation [9], as (0.4 + 0.09 *B [T]) [nΩ·m], and the twist pitch of the filament, p, is equal to 6.6 mm, as from specifications. The figure 37 shows the magnetization map for the interfilament coupling currents and the associated power loss on the conductor blocks.

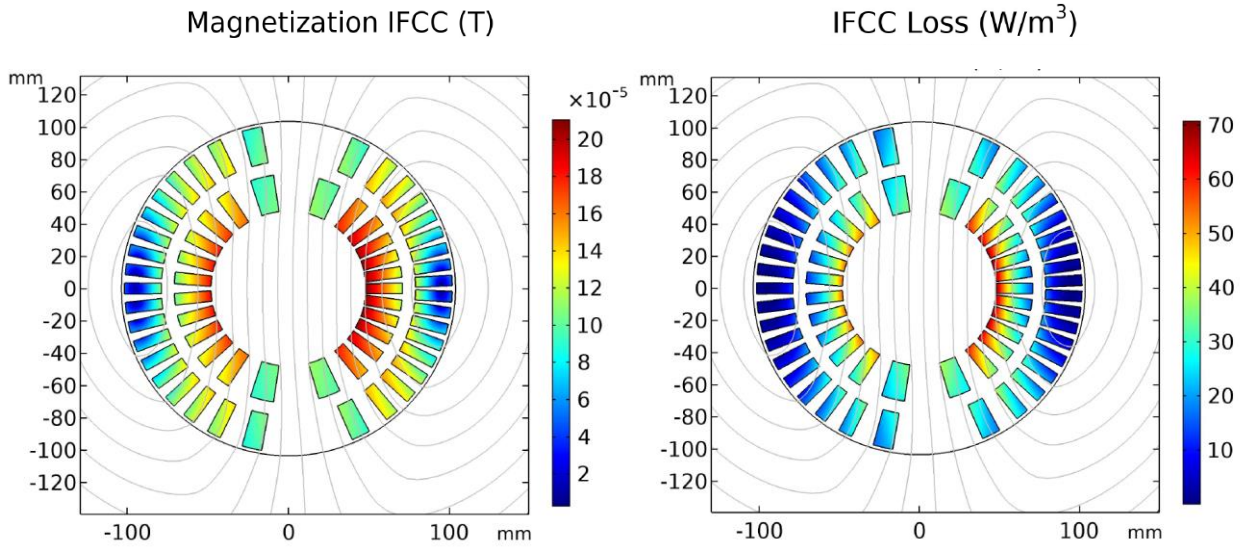

Figure 5. Magnetization, M_{IFCC} and power density, P_{IFCC}, maps generated by the interfilament coupling currents at nominal field of 4 T.

6.1.3 Total conductor losses

In order to evaluate the power losses per unit length, the power densities presented in the previous paragraphs are integrated on the conductor block surfaces. The results are reported in Tab. 16 for three different bore field B_0 (0.45, 2 and 4 T). The figure 38 plots the power losses per unit length versus the bore magnetic field of the CCT magnet. The figure highlights that the biggest contribution is given by the persistent currents and the highest contribution of power losses at low field (B_0=0.45 T) is not negligible for the thermal design. The thermal conductivity of a metallic former could help to take out the heat generated by these losses, linking the former to the cryocooler.

In this preliminary analysis the interstrand coupling currents losses haven't been considered, because they give the lowest contribution to the conductor power losses, as for the Rutherford cable [ref.], but they will be integrated in a future analysis.

Table 16. Conductor power losses per unit length versus the bore magnetic field.

I [A] - rope	B_0 [T]	P_{PC} [W/m]	P_{IFCC} [W/m]	P_{TOT} [W/m]
146	0.45	1.896	0.428	2.324
650	2	0.908	0.345	1.253
1308	4	0.619	0.261	0.880

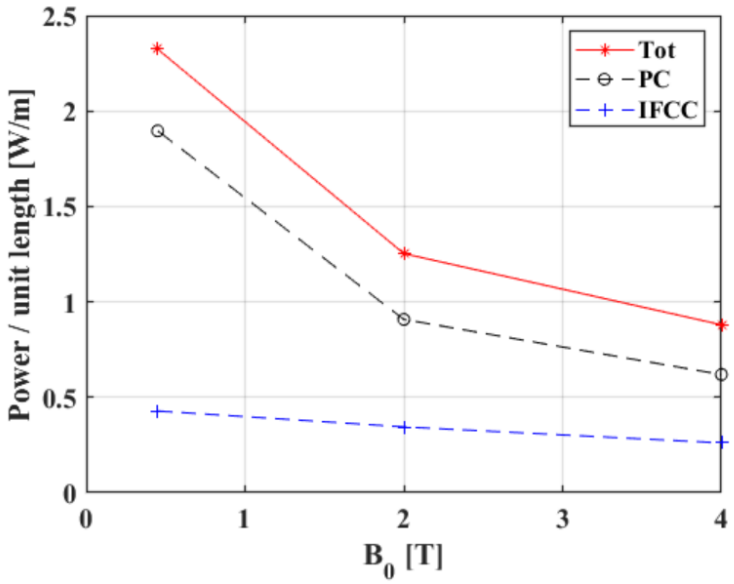

Figure 38. Power losses per unit length in the conductors over the coils cross section: PC, persistent currents losses, IFCC, interfilament coupling currents losses, and TOT, total losses.

6.2 METALLIC FORMER LOSSES

As presented in the section 3, one of the materials studied for the former is the aluminium bronze. Considering the fast ramp rate of the field, 0.4 T/s, the eddy current foreseen in a metallic former are not negligible. In the following subsection the metallic former losses are presented, and in particular the focus is on the evaluation of the eddy currents and the associated power losses per unit length.

The evaluation is split in two parts: one for the inner former and the other for the outer one. Indeed, the two formers during the ramp are subjected to different magnetic fields: the inner one by the transversal dipolar field (plane x, y) of the two former coils, and the outer one by a dipole field plus the longitudinal (solenoidal) field generated by the only outer former coil (see Fig. 39). Another assumption is to consider just the bulk tube of the formers without the ribs (Fig. 39), where the eddy currents cannot flow azimuthally. The evaluation of the eddy currents has been done in two different former layouts: the first with bulk formers, and the second with formers cut on the pole in order to have two insulating halves and to split the path of the eddy currents.

6.2.1 Inner layer eddy current losses

For the inner layer, as abovementioned, the dipolar field ramp, dB_y/dt induces a longitudinal electrical field, E_z, defined as:

$$B_y = -\frac{dA_z}{dx}$$

$$A_z = -xB_0$$

$$E_z = -\frac{dA_z}{dt} = x\,\dot{B}_0 = r\,cos(\theta)\,\dot{B}_0 \tag{14}$$

where A_z is the potential vector, and B_0 is the transversal dipolar field. The eddy current density generated is

$$J_z = \frac{E_z}{\rho} = \frac{r\,cos(\theta)\,\dot{B}_0}{\rho} \tag{15}$$

The volumetric power density is defined as the electrical field E_z to the power of two divided the resistivity of the former material:

$$p = \frac{E_z^2}{\rho} = \frac{r^2\,\cos(\theta)^2\,\dot{B}_0^2}{\rho} \tag{16}$$

The power losses per unit length is the volumetric power density integrated between the radii of the former (R_1 and R_2, Fig. 39), and the radial angle:

$$P/_l = \int_{R_1}^{R_2}\int_0^{2\pi} p\,r\,dr\,d\theta = \frac{\left(R_2^4-R_1^4\right)\dot{B}_0^2\,\pi}{4\rho} \tag{17}$$

If the former is cut on the pole, splitting the eddy current in two, the previous formula becomes:

$$P/_l = \frac{\left(R_2^4-R_1^4\right)\dot{B}_0^2\,\pi}{4\rho}\left(1-\frac{8}{\pi^2}\right) \tag{18}$$

leading to a reduction of losses of 80%.

6.2.2 Outer former eddy current losses

Regarding the eddy currents generated into the outer former, as mentioned in the introduction, the outer former is subjected to different magnetic fields: the dipolar field from the inner former coil, the dipolar field from the outer former coil, and the solenoidal component of the outer coil, not compensated in the region of the outer former. From this, the associated power per unit length for a bulk outer former is the sum of two contributions:

$$P_{tot}/_l = {P_{z,tot}}/_l + {P_\vartheta}/_l \tag{19}$$

where $P_{z,tot}/l$ is the contribution from the two transversal dipolar fields and P_ϑ/l is the contribution from the solenoidal field. Avoiding the intermediate steps to derive them, the explicit formulas for the two aforementioned contributions in the case of bulk formers are

$${P_{z,tot}}/_l = \frac{\dot{B}o^2}{4\rho}\pi\left[\frac{\left({R_4}^4-{R_3}^4\right)}{4} + {R_c}^2\left({R_4}^2-{R_3}^2\right) + {R_c}^4 ln\left(\frac{R_4}{R_3}\right)\right] \tag{20}$$

$${P_\vartheta}/_l = \frac{\dot{B}_0^2}{4\rho}\pi\left[\frac{\left({R_4}^4-{R_3}^4\right)}{4} - {R_c}^2\left({R_4}^2-{R_3}^2\right) + {R_c}^4 ln\left(\frac{R_4}{R_3}\right)\right]2\tan(\alpha)^2 \tag{21}$$

where $\dot{B}o$ is the transversal dipolar field derivative in time, R_4 and R_3 are the maximum and minimum radius of the outer former tube (Fig. 39), R_c is the average radius of the inner former tube and ρ is the former material resistivity. The losses from the solenoidal field account for 15% of the total loss, while the largest contribution is from the dipole fields.

In the case of formers cut on the pole, the previous formulas become

$$P_{z,tot}/_l = \frac{\dot{B}_0^2}{4\rho}\pi\left[\frac{({R_4}^4-{R_3}^4)}{4} + {R_c}^2({R_4}^2-{R_3}^2) + {R_c}^4 ln\left(\frac{R_4}{R_3}\right)\right]\left(1-\frac{8}{\pi^2}\right) \quad (22)$$

$$P_\vartheta/_l = 0$$

in which the power losses per unit length from the transversal dipolar fields are reduced of 80% and the ones from the solenoidal field are cancelled out.

6.2.3 Evaluation of former eddy current power losses

The evaluation of eddy current power losses has been done for different former materials and for the parameters reported in Tab. 17. Figure 39 shows the distribution of the eddy currents and of the volumetric power losses on the two formers tube cross section in the case of aluminium bronze formers. From the figure 39, it's clear the reduction of eddy current density and volumetric power losses in the case of formers cut on the pole (Fig.39, right side) with respect to the bulk formers (Fig. 39, left side).

Table 17. CCT magnet parameters for former eddy currents power losses evaluation

$\dot{B}_0$ [T/s]	R1 [mm]	R2 [mm]	R3 [mm]	R4 [mm]	T_{op} [K]
0.4	40	48	73	81	4.5

The evaluation of the power losses per unit length has been done for different metals as reported by Tabs. 18 and 19. The best choice from the results is represented by the stainless steel AISI-316 for both the case studies (bulk and cut ones). From feedbacks of the machining experts the use of stainless steel for this kind of formers is very complicated. The alternative solution could be to use the aluminium-bronze for the former cut on the pole, in order to keep the power losses to be dissipated in the order of 2 W/m.

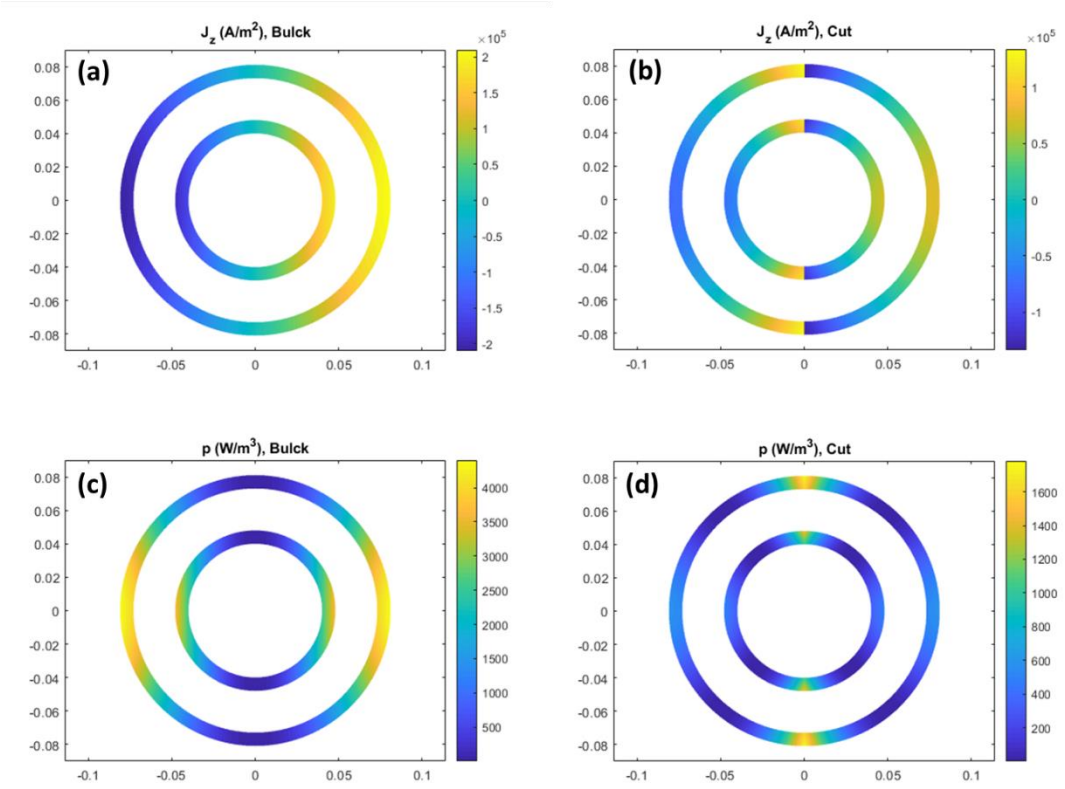

Figure 6. Eddy currents and volumetric power losses on the two formers tube cross section in the case of aluminium bronze formers. On the left side the eddy currents J_z (a) and the associate volumetric power distribution (c) are shown for the bulk former case. On the right side the eddy currents Jz (b) and the associate volumetric power distribution (d) are shown for the former cut on the pole.

Table 18. Power losses per unit length in the case of bulk formers for different metals.

Metal	ρ [Ω*m]	P_{inner} [W/m]	P_{outer} [W/m]	P_{tot} [W/m]
Pure aluminium (RRR=10)	2e-9	173	474	647
Aluminium 6061	1.38e-8	25	69	94
Bronze	7.3e-8	4.7	13	18
Aluminium-Bronze	1e-7	3.5	9.5	13
AISI-316	5e-7	0.7	1.9	2.6

Table 19. Power losses per unit length in the case of formers cut on the pole for different metals.

Metal	ρ [Ω*m]	P_{inner} [W/m]	P_{outer} [W/m]	P_{tot} [W/m]
Pure aluminium (RRR=10)	2e-9	33	77	110
Aluminium 6061	1.38e-8	4.7	11	16
Bronze	7.3e-8	0.9	2.1	3
Aluminium-Bronze	1e-7	0.7	1.5	2.2
AISI-316	5e-7	0.13	0.31	0.44

6.3 CURRENT LEADS POWER CONSUMPTION

The current leads power consumption is another point to explore for the CCT demonstrator presented, especially for an operation temperature of 4.7 K, that foresees the use of helium gas cooled by cryocoolers. The main idea is to use an HTS conduction-cooled current lead (Fig. 40), composed of a resistive lead with an intermediate heat sink as the top part of the HTS lead.

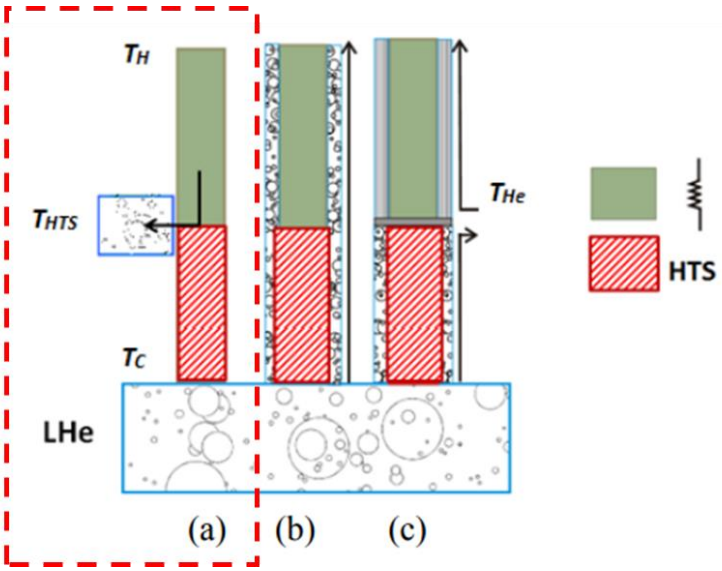

Figure 40. HTS current leads: cooling scheme for (a) HTS conduction-cooled current lead; (b) HTS self-cooled current lead; and (c) HTS gas-cooled current lead.

The configuration of the CCT magnet is shown in the Fig. 41, where the current leads consist of a copper resistive part between room temperature and 60 K, and an HTS part between 60 K and 4.7 K. The 60 K temperature should be provided by a cryo-cooler, which acts as heat-sink for the upper resistive part of the leads.

As presented in [23], the power consumption for a conduction-cooled current lead is calculated by solving the steady-state heat balance equation, when the length of the current lead, L is much bigger than the cross section, A (L>>A):

$$\frac{\mathrm{d}}{\mathrm{d}T}\left(k(T)A\frac{\mathrm{d}T}{\mathrm{d}x}\right)+\rho(T)\frac{1}{A}I^2=0$$

where ρ(T) is the electrical resistivity in function of the temperature, k(T) is thermal conductivity of the current lead material and $Q(T)=k(T)A\frac{dT}{dx}$ is the heat conducted. If the heat inleak at the cold end is indicated with Qc, the solution of the abovementioned equation is

$$Q_C=\sqrt{Q_H^2+L_0I^2(T_H^2-T_C^2)}\quad[\mathrm{W}]$$

where L_0 is the Lorenz number, I is the current flowing, Q_H is the heat at the hot end, T_H and T_C are the temperatures of the warm and cold end of the current leads. If the heat conducted at the warm end of the lead is equal to zero ($Q_H = 0$) the solution becomes:

$$\frac{Q_{C,min}}{I} = \sqrt{L_0(T_H^2 - T_C^2)} \quad [\text{W/A}]$$

Explicating the solution just for the resistive part of the case shown in Fig. 41, the equivalent heat between 300 K and 60 K is

$$\frac{Q_{C,min}}{I} = 46 \quad [\text{W/kA}]$$

and for a rope current of 1300 A, $Q_{C,min} \sim 60\ W$ for each current lead, i.e. 120 W of cooling power to be supplied by one cryocooler just for the current leads. Other comment is that the same current lead at zero current absorbs the 50% of the nominal power (nominal current) if made by phosphorus deoxidized copper (much more if made by pure copper).

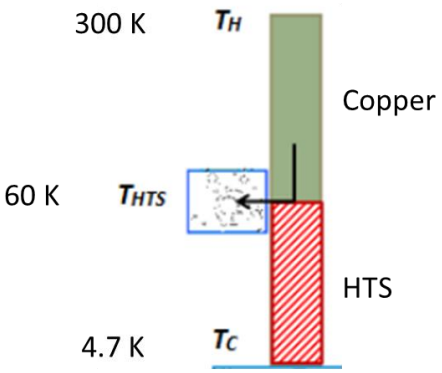

Figure 41. HTS conduction-cooled current lead for the CCT magnet demonstrator.

7. Conclusions and future plans

The conceptual design report of the combined CCT demonstrator in NbTi, represents a preliminary study of the magnet from the magnetic, mechanical, protection and power losses point of view.

The list of the parameters (target, superconductor, cable and CCT inner and outer layers) have been presented, motivating the design choice for the majority of the values.

The magnetic design section shows the magnetic performance at nominal current (@ 4.7 K) of the combined CCT, and how it achieves the target dipole and quadrupole fields, reporting also the field quality in terms of normal harmonics bn. The load line margin at the nominal current and at 4.7 K of operational temperature is of 28.7% and 33.4% at 4.2 K (liquid helium). The critical temperature is 6.3 K giving a temperature margin of about 1.6 K. The magnetic length is of about 0.73 m, less than target one (0.8 m, Tab.1), which is perfectly acceptable.

The mechanical design presents a full description of the mechanical structure. The materials simulated for the former are aluminium bronze 954 and PEEK GF30 (polyether-ether-ketone reinforced with 30% of glass fibres). The stresses on the formers are well below the limit of both materials, resulting in a safety factor of 1.67 for PEEK GF 30 and 2.37 for aluminium bronze 954. The stresses on the conductor are far from the yield limit of 300 MPa of Nb-Ti. In case of aluminium bronze 954, the radial displacements are of the order of 10 µm, while for PEEK GF30 they are of about 100 µm (to be verified if critical or not). Azimuthal displacements have been evaluated but they remain well below the 100 µm for both the materials. So far both materials are kept as candidate for the former.

The protection section highlights that the time margins are very large (0.325 s for a rope 6 NbTi+1 copper strands, and 0.149 s for a rope 7 NbTi strands). The rope (6 NbTi +1 copper strands) has been selected.

For ramped field (0.4 T/s), the conductor losses, persistent and interfilament coupling currents, are bigger than 2 W/m at low field (0.45 T), while are less than 1 W/m at 4 T. The eddy currents losses from the metallic former are the most significant ones, especially if the bulk formers are considered (13 W/m for the aluminium bronze). We think to start with Al bronze, however ready to switch to PEEK if possible. The preliminary calculation of the current leads power consumption for a rope current of 1300 A gives 120 W of cooling power at 50 K to be supplied by one cryocooler.

A more detailed study covering all the open points will be done for the final Engineering Design report. By that time, we will have made the final decision between aluminium bronze and PEEK. This last is better for losses but need to be proved in term of mechanical stability.

In conclusion we have now a solid base to go for a more detailed design and then demonstrator construction.

8. References

[1] European Commission Directorate-General for Research and Innovation, (2021) Grant Agreement Number 101004730 - I.FAST.

[2] Rossi, L., Ballarino, A., Barna, D., Benedetto, E., Calzolaio, C., Ceruti, G., ... & Vieweg, M. (2022). A European collaboration to investigate superconducting magnets for next generation heavy ion therapy. IEEE Transactions on Applied Superconductivity.

[3] Bermudez, S. I., Nilsson, E., Bottura, L., Bourcey, N., Devred, A., Ferracin, P., ... & Willering, G. (2019). Mechanical analysis of the Nb3Sn 11 T dipole short models for the High Luminosity Large Hadron Collider. *Superconductor Science and Technology*, 32(8), 085012.

[4] Vallone, G., Anderssen, E., Bordini, B., Ferracin, P., Troitino, J. F., & Prestemon, S. (2020). A methodology to compute the critical current limit in Nb3Sn magnets. *Superconductor Science and Technology*, 34(2), 025002.

[5] Ekin, J. W. (1978). Fatigue and stress effects in NbTi and Nb3Sn multifilamentary superconductors. In Advances in Cryogenic Engineering (pp. 306-316). *Springer*, Boston, MA.

[6] De Matteis, E., & I.FAST WP8 members. (2022) Characterization of the first length of superconductor for low losses, *Zenodo*. https://doi.org/10.5281/zenodo.5901601

[7]HITRIplus. (2021) Heavy Ion Therapy Research Integration. [Online]. Available: https://www.hitriplus.eu/

[8] Amaldi, U., Alharbi, N., Riboni, P., Karppinen, M., Perini, D., Le Godec, G., ... & Benedetto, E. (2021). Sigrum-A Superconducting Ion Gantry With Riboni's Unconventional Mechanics (*No. CERN-ACC-NOTE-2021-0014*).

[9] Alessandria, F., Angius, S., Bellomo, G., Fabbricatore, P., Farinon, S., Gambardella, U., Marabotto, R., Musenich, R., Repetto, R., Sorbi, M., Volpini, G. (2009) Technical design report of a superconducting model dipole for FAIR SIS300, *INFN/code-08/001* https://air.unimi.it/handle/2434/72640

[10] Rossi, L. (2002). State-of-the-art superconducting accelerator magnets. *IEEE transactions on applied superconductivity*, 12(1), 219-227.

[11] Caspi, S., Borgnolutti, F., Brouwer, L., Cheng, D., Dietderich, D. R., Felice, H., ... & Wang, X. (2013). Canted–Cosine–Theta magnet (CCT)—A concept for high field accelerator magnets. *IEEE Transactions on Applied Superconductivity*, 24(3), 1-4.

[12] Kirby, G. A., Rysti, J., Gentini, L., Van Nugteren, J., Murtomäki, J., De Rijk, G., ... & Perez, J. C. (2016). Hi-Lumi LHC twin-aperture orbit correctors magnet system optimisation. *IEEE transactions on applied superconductivity*, 27(4), 1-5.

[13] Dassault Systemes, OPERA-SIMULIA, https://www.3ds.com/products-services/simulia/products/opera/

[14] Bottura, L. (2000). A practical fit for the critical surface of NbTi. *IEEE transactions on applied superconductivity*, 10(1), 1054-1057.

[15] Lubell, M. (1983). Empirical scaling formulas for critical current and critical field for commercial NbTi. *IEEE Transactions on magnetics*, 19(3), 754-757.

[16] Italian Government. (2009) TESTO UNICO SULLA SALUTE E SICUREZZA SUL LAVORO (TEXT ON HEALTH AND SAFETY IN THE WORKPLACE). *D.lgs. 81/08*.

[17] Bottura, L. (1997) Standard Analysis Procedures for Field Quality Measurement of the LHC Magnets - Part I: Harmonics, CERN, *LHC Project Report*, MTA-IN-97-007.

[18] Ortwein, R., Blocki, J., Wachal, P., Kirby, G., & van Nugteren, J. (2020). FEM modeling of multilayer Canted Cosine Theta (CCT) magnets with orthotropic material properties. *Cryogenics*, 107, 103041

[19] Chu, X. X., Wu, Z. X., Huang, R. J., Zhou, Y., & Li, L. F. (2010). Mechanical and thermal expansion properties of glass fibers reinforced PEEK composites at cryogenic temperatures. *Cryogenics*, 50(2), 84-88.

[20] Drake Plastics Ltd. Co., KetaSpire® PEEK Design & Processing Guide.

[21] Rossi, L., & Sorbi, M. (2005). MATPRO: a computer library of material property at cryogenic temperature (*No. CARE-NOTE-2005-018-HHH*). https://cds.cern.ch/record/941440/files/note-2005-018-HHH.pdf

[22] WILSON, Martin N. (1983) *Superconducting magnets*. Oxford: Clarendon Press.

[23] Ballarino, A. (2015) Current leads, links and buses. *arXiv preprint arXiv:1501.07166*.